ACS OMEGA

http://pubs.acs.org/journal/acsodf

Article

Targeted and Enhanced Antimicrobial Inhibition of Mesoporous ZnO−Ag_2O/Ag, ZnO−CuO, and ZnO−SnO_2 Composite Nanoparticles

Monica Pandey, Monika Singh, Kirti Wasnik, Shubhra Gupta, Sukanya Patra, Prem Shankar Gupta, Divya Pareek, Nyshadham Sai Naga Chaitanya, Somedutta Maity, Aramati B. M. Reddy, Ragini Tilak, and Pradip Paik*

Cite This: *ACS Omega* 2021, 6, 31615−31631

Read Online

ACCESS | Metrics & More | Article Recommendations | Supporting Information

ABSTRACT: In this work, mesoporous (pore size below 4 nm) composite nanoparticles of ZnO−Ag_2O/Ag, ZnO−CuO, and ZnO−SnO_2 of size $d \leq 10$ nm (dia.) have been synthesized through the *in situ* solvochemical reduction method using $NaBH_4$. These composite nanoparticles exhibited excellent killing efficacy against Gram-positive/negative bacterial and fungal strains even at a very low dose of 0.010 μg/mL. Additionally, by applying the *in silico* docking approach, the nanoparticles and microorganism-specific targeted proteins and their interactions have been identified to explain the best anti-bacterial/anti-fungal activities of these composites. For this purpose, the virulence and resistance causing target proteins such as *PqsR*, *RstA*, *FosA*, and *Hsp90* of *Pseudomonas aeruginosa*, *Acinetobacter baumannii*, *Klebsiella pneumoniae*, and *Candida albicans* have been identified to find out the best inhibitory action mechanisms involved. From the *in vitro* study, it is revealed that all the composite nanoparticle types used here can act as potent antimicrobial components. All the composite nanoparticles have exhibited excellent inhibition against the microorganisms compared to their constituent single metal or metal oxide nanoparticles. Among the nanoparticle types, the ZnO−Ag_2O/Ag composite nanoparticles exhibited the best inhibition activity compared to the other reported nanoparticles. The microorganisms which are associated with severe infections lead to the multidrug resistance and have become a huge concern in the healthcare sector. Conventional organic antibiotics are less stable at a higher temperature. Therefore, based on the current demands, this work has been focused on designing inorganic antibiotics which possess stability even under harsh conditions. In this direction, our developed composite nanoparticles were explored for potential uses in the healthcare technology, and they may solve many problems in global emergency and epidemics caused by the microorganisms.

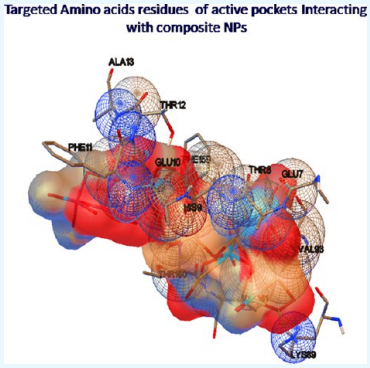

INTRODUCTION

Microbial contamination, adhesion, persistence colony formation on surfaces, and associated infections have become detrimental to public health and are causing massive alarm.[1] The over usages of antibiotics lead to the development of resistant microbial strains which are the main cause of the antimicrobial resistance and persistent infection.[2] Thus, there is a high demand of efficient antimicrobial components that can resist the infection level. There are many organic, inorganic, and polymeric antibiotics, and each of them has their own advantages and disadvantages. Organic and polymeric antimicrobial agents are very much temperature sensitive, possess shorter lifetime, can degrade easily, and manifest various side effects in the long run.[3] Therefore, constant efforts are necessary toward the development of new antimicrobial components to address these challenges with minimum side effects.

In the recent trends, nanoparticles (NPs) have also been explored as an efficient antimicrobial component mainly due to their unique mechanism of action, contact killing effect, the generation of reactive oxygen species (ROS), disruption of DNA, disruption of cell membrane, and so forth.[2,4−9] However, the field of material research is constantly progressing to accomplish the best antibiotics with optimum results. Materials such as metal and metal oxide NPs like ZnO (zinc oxide),[5] CuO (copper oxide),[10] SnO_2 (tin oxide),[11] and Ag_2O (silver oxide)[12,13] NPs and different polymeric NPs have been reported and used for their antimicrobial properties. However, metallic/metal oxide NPs have been experimented and reported for the antimicrobial properties since time immemorial due to their unique way of interactions with the cellular components. By interacting with the thiol groups of enzymes, metallic/metal oxide NPs inactivate the cellular activities of proteins.[14] Hence, further development of inorganic antimicrobial agents such as metal and metal oxide

Received: August 3, 2021
Accepted: November 8, 2021
Published: November 16, 2021

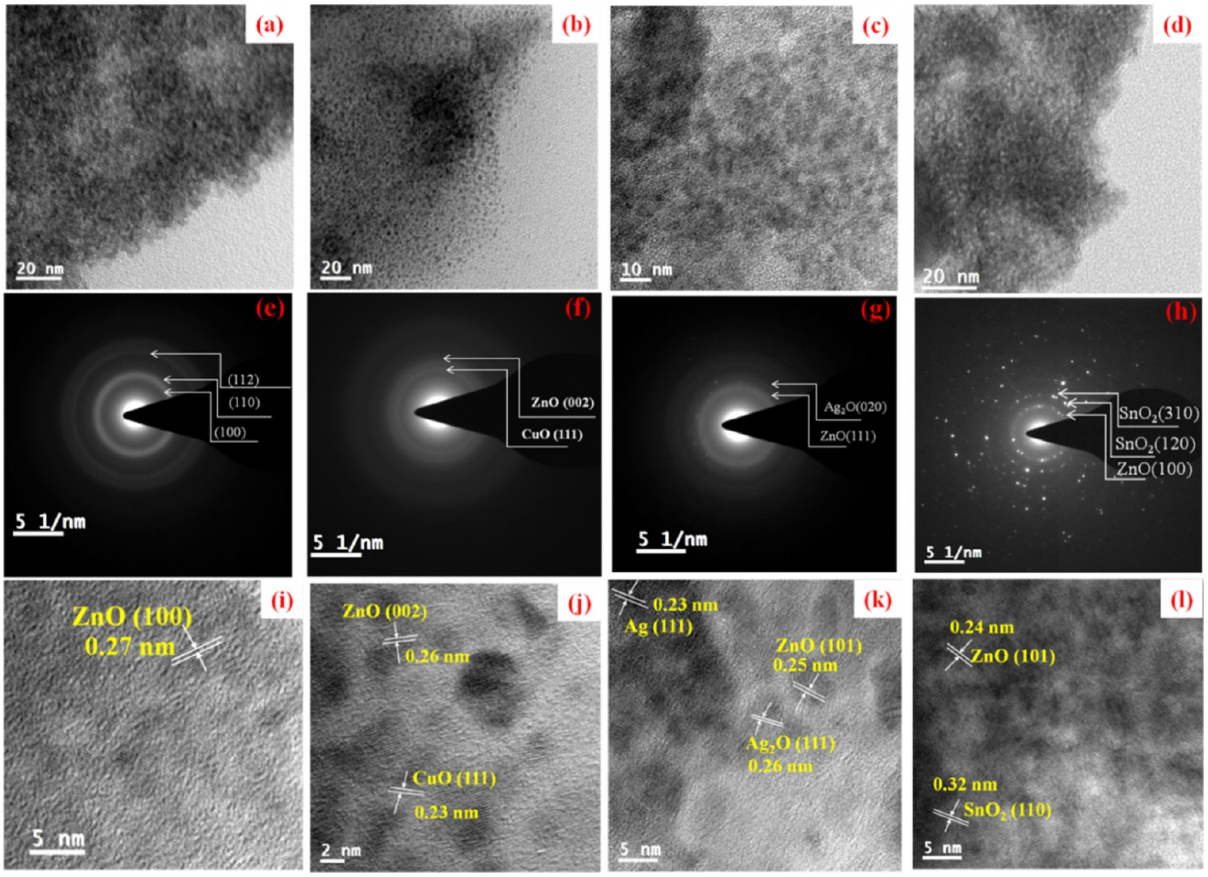

Figure 1. HRTEM micrographs for (a) ZnO, (b) ZnO−CuO, (c) ZnO−Ag_2O/Ag, and (d) ZnO−SnO_2; SAED pattern for (e) ZnO, (f) ZnO−CuO, (g) ZnO−Ag_2O/Ag, and (h) ZnO−SnO_2; and *d*-spacing for (i) ZnO, (j) ZnO−CuO, (k) ZnO−Ag_2O/Ag, and (l) ZnO−SnO_2.

NPs could become an alternative simple and cost-effective strategy to address the problems related to the microbial infections and associated issues.

Furthermore, many researchers have explored metallic oxides for their wide applications, especially for antimicrobial efficiency. For example, ZnO NPs were used for electronic applications and to control the infection of both Gram-positive[15] and Gram-negative bacteria.[15−17] SnO_2 NPs due to their wide band energy gap (E_g ∼ 3.6 eV) are used for photocatalytic properties and have been explored in antibacterial activities too. Similarly, antibacterial activities of Ag and Ag_2O NPs have been widely studied against different bacterial strains, for example, *Listeria monocytogenes* (*L. monocytogenes*), *Escherichia coli* (*E. coli*), *Salmonella typhimurium,* and *Vibrio Parahaemolyticus* (*V. parahaemolyticus*). However, the effective rate of antibacterial properties depends on the size, shape, and morphology of the Ag NPs.[18,19] Similarly, antibacterial activity of CuO NPs has been studied against *Pseudomonas aeruginosa* (*P. aeruginosa*), *Klebsiella pneumonia* (*K. pneumonia*), *Salmonella paratyphi* (*S. paratyphi*), and *Shigella flexneri* (*Staphylococcus flexneri*) strains, and so forth.[20,21] It has been noted that the particle size-dependent antimicrobial activities[22] against *Staphylococcus aureus* (*S. aureus*), *Bacillus subtilis* (*B. subtilis*), *Pseudomonas aeruginosa* (*P. aeruginosa*), and *E. coli* are also reported and found that this anti-bactericidal efficiency follows the order: ZnO > CuO > Fe_2O_3. The zone of inhibition (ZOI) for ZnO NPs obtained is highest, *ca.* 25 mm against *B. subtilis* and *ca.* 19 mm against *E. coli*. Thus, many antimicrobial single oxide NPs are demonstrated; however, current situation demands newer materials for better efficacy than the reported results.[3] Presently, researchers have also focused toward the combination of two or more metals/metal oxide NPs for many purposes such as photocatalytic activity,[23] antibacterial purposes,[24−27] making optical devices,[28] and energy harvesting,[29] to solve the environment issues[27] and so forth. These NPs can be synthesized through various methods, for example, solvothermal, sol−gel, microwave assisted, and so forth. It has also been noticed that antimicrobial properties of NPs depend on the size, shape, morphology, and the synthetic methods. Basically during the development of metal oxide, metal alloy and metal/metal oxide, cooperative exchange of charges among the mixed oxide or metals/alloys[30] and difference in the electronic potential/energy band gap have been observed. Hence, it is considered that combination of two or more metals/metal oxide could provide significant results in the treatment of microbial strains efficiently. Furthermore, researchers have explored the mixed metal oxide composites, for example, $CaCO_3$/MgO against *S. aureus* and *E. coli*,[31] mixed ZnO−MgO component against *B. subtilis* and *E. coli*,[32] and bimetallic Ag−Cu NPs[33] against the *C. albicans*, *E. coli*, and *S. aureus*, which showed both bacteriostatic and bactericidal activities and exhibited lower anti-fungicidal activities.

Thus, the challenges of present situation are to find out newer broad spectrum antimicrobial agents, which will be having efficient microbial killing efficacy within minimum dose, without exhibiting side effects and having longer stability. In the present context of the healthcare demands, the objective of

https://doi.org/10.1021/acsomega.1c04139
ACS Omega 2021, 6, 31615−31631

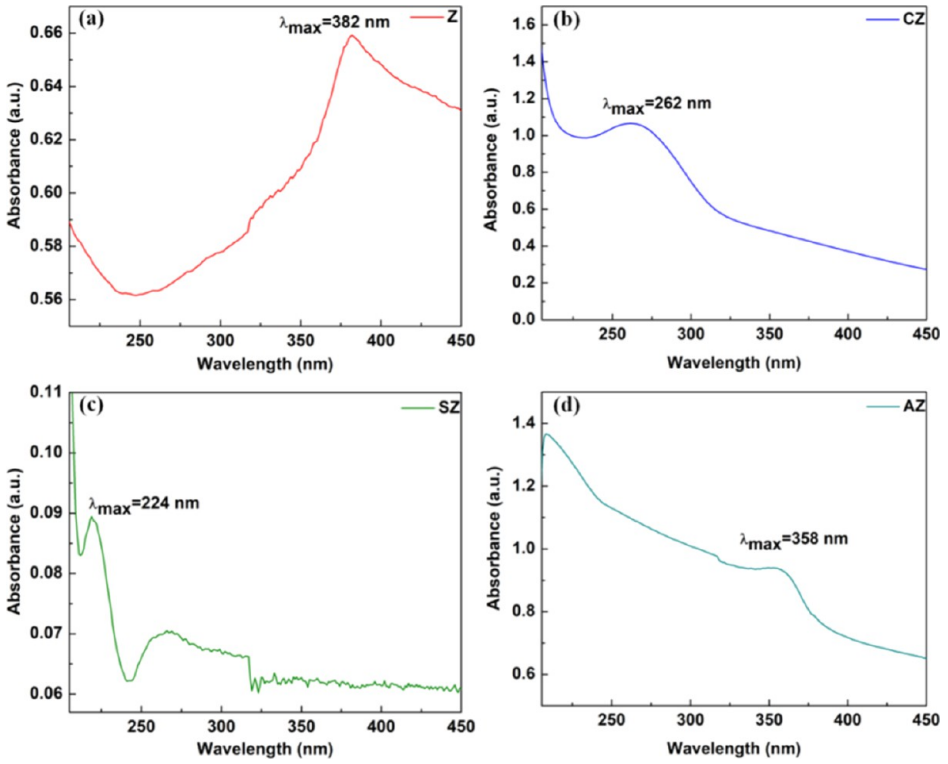

Figure 2. UV−vis spectra of composite NPs: (a) ZnO NPs, (b) ZnO−CuO NPs, (c) ZnO−SnO_2 NPs, and (d) ZnO−Ag_2O/Ag NPs.

this work is to synthesize mixed oxide/composites such as ZnO−CuO, ZnO−Ag_2O/Ag, and ZnO−SnO_2NPs with smaller size and with porous structure by the *in situ* chemical reduction method to achieve very high surface area-to-volume ratio and effective antimicrobial activities. Furthermore, docking prediction has been performed to evaluate and predict the interactions of the composite NPs for their enhanced activity compared to the single metal/metal oxide NPs. It has also been observed that NPs could act as a potential antimicrobial agent against the drug-resistant microorganisms. Furthermore, it has also been observed that in microorganism resistance development, enhanced virulence capacity, biofilm formation, and quorum-sensing mechanisms are regulated by the various proteins. Such as, (i) PqsR is involved in the quorum-sensing pathway of *P. aeruginosa*, and it controls virulence,[34] and (ii) FosA gene and RstA (BfmR) are involved in controlling the stress response and multidrug resistance issues.[35] It has been observed that FosA gene was found in seven types of *E. coli* pathogenic strains,[36] which controls the metabolization of fosfomycine via regulating expression of metal-dependent glutathione transferase.[37] It is known that the *Klebsiella pneumoniae* and *P. aeruginosa* are inherently resistant to fosfomycine, while in *Acinetobacter baumannii* stain, BfmR is a conserved gene. Interestingly, targeting to BfmR, it can decrease the survival of *A. baumannii*, and it can increase the sensitivity of organism toward the antimicrobial and antibiofilm formation.[38] In candida, conserved molecular chaperone Hsp90 governs the key functions like thermal stability, cell cycle regulation, morphogenesis, expression of virulence trait, and drug resistance.[39] Therefore, for the conformation of enhanced antibacterial and antifungal activities of metallic nanocomposite, we have carried out interaction studies using the quorum-sensing proteins PqsR,[34] RstA response regulator,[38] and resistance causing FosA proteins.[37] Then, *in vitro* differential antibacterial and antifungal activities have been studied in this work by the KB test. The efficacies of inhibiting the microorganism of our materials have been evaluated by calculating the minimum inhibitory concentration (MIC) and the ZOI in different strains. Additionally, we have tested the antimicrobial properties of individual metal oxide such as ZnO, Ag_2O/Ag, CuO, and SnO_2 NPs separately, which were synthesized using the same approach. Finally, the antimicrobial properties of Ag_2O, CuO, SnO_2, and ZnO NPs and ZnO−CuO, ZnO−AgO_2/Ag, and ZnO−SnO_2 NPs have been compared using the *in silico* and *in vitro* studies. Thus, in the present study, we have focused mainly on the composite NPs doped with metal/metal oxide NPs, and their antimicrobial results were compared with the ZnO NPs which could challenge differently the microorganism-based infections and diseases.

RESULTS AND DISCUSSION

The ZnO−CuO, ZnO−Ag_2O/Ag, and ZnO−SnO_2 NPs were synthesized by the *in situ* solvochemical reduction method using $NaBH_4$ as mentioned in the Experimental Section. Detailed synthesis methods for different samples have been filed for patents.[40,41] The HRTEM micrographs of ZnO, ZnO−CuO, ZnO−Ag_2O/Ag, and ZnO−SnO_2 NPs are shown in Figure 1a−d, respectively, where all the NPs are observed in well dispersed form. Size and morphology of the NPs are observed form HRTEM (Figure 1) which shows ZnO NPs are quasi-spherical in shape with average size of *ca.* 2.25 ± 0.3 nm in diameter. The ZnO−CuO NPs (Figure 1b) shows an average size of 2.1 ± 0.2 nm in diameter. The mono dispersed ZnO−Ag_2O/Ag NPs (Figure 1c) are of the size 3.2 ± 0.2 nm in diameter and ZnO−SnO_2 NPs (Figure 1d) are of the size 5 ± 0.2 nm in diameter. The selected area electron diffraction (SAED) pattern for ZnO, ZnO−CuO, ZnO−Ag/Ag_2O and

https://doi.org/10.1021/acsomega.1c04139
ACS Omega 2021, 6, 31615−31631

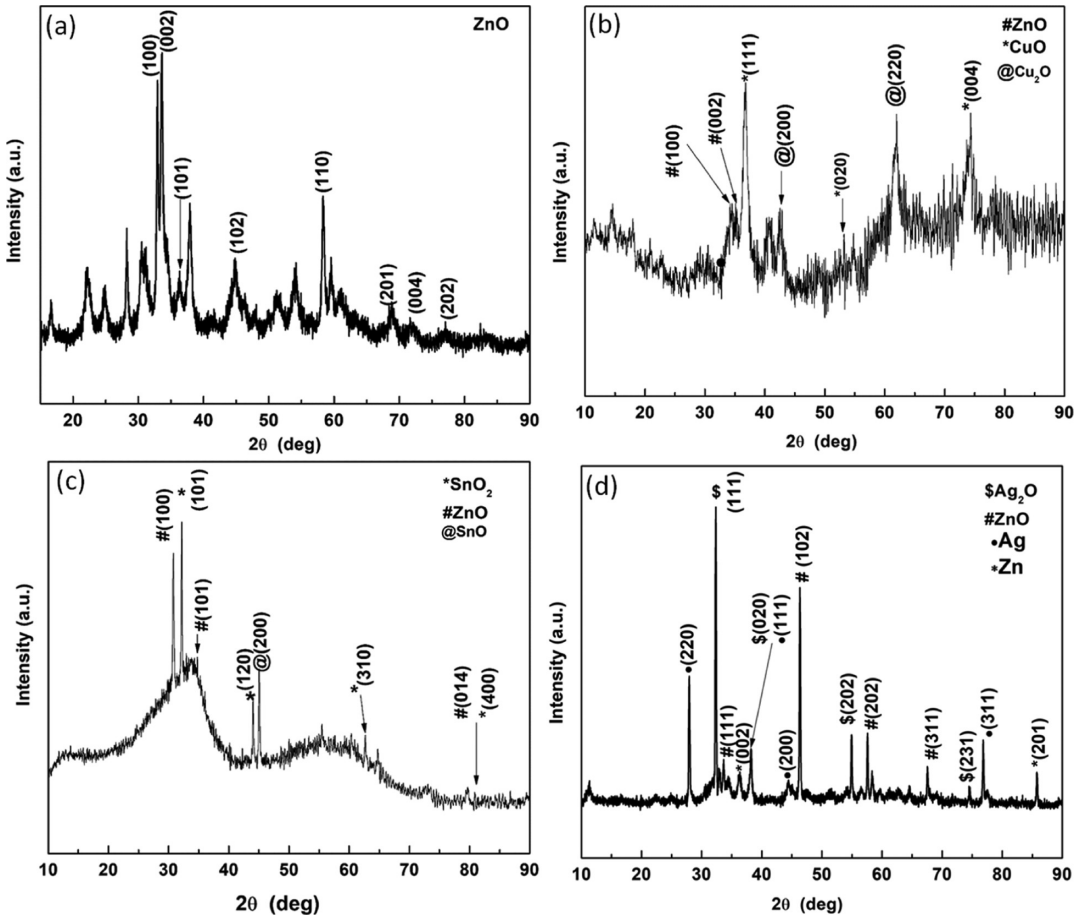

Figure 3. XRD patterns of (a) ZnO, (b) ZnO−CuO, (c) ZnO−SnO_2, and (d) ZnO−Ag_2O/Ag NPs.

ZnO−SnO_2 are shown in Figure 1e−h, respectively. The *d*-spacing values were calculated from HRTEM image and it is found to be 0.27 nm corresponds to the ZnO(100) (as shown in Figure 1i) and this value is matching well with the pure ZnO NPs. For ZnO−CuO, the *d*-spacing is calculated to be 0.23 nm for CuO(111) and 0.26 nm for ZnO(002), as shown in Figure 1j. For ZnO−Ag_2O/Ag, the *d*-spacing ∼0.25 nm corresponds to ZnO(101), 0.23 nm for Ag(111) and 0.26 nm for Ag_2O(111), as shown in Figure 1k. For ZnO−SnO_2, *d*-spacing is calculated to be 0.24 nm for ZnO(102) and 0.32 nm corresponding to the SnO_2(110), as shown in Figure 1l. Thus, the samples are mixed oxide components. These results are in well agreement with the X-ray diffraction (XRD) results which are represented in the subsequent section.

The UV−visible spectra were acquired in the range of 190−800 nm for all the NPs to find out the surface plasmon behavior (Figure 2). All the samples exhibited a single distinct absorption band at 382 nm (Figure 2a), 262 nm (Figure 2b), 224 nm (Figure 2c), and 358 nm (Figure 2d) for ZnO, ZnO−CuO, ZnO−SnO_2, and for ZnO−Ag_2O/Ag, respectively. The appearance of a single absorption band instead of double peaks denotes that the bimetallic-oxide composites have been formed in the presence of $NaBH_4$, which are further converted into oxides since the synthesis process was conducted in the oxidizing environment, and the overall composition of the various samples is in agreement with the uniformly mixed phase.[42] Another important fact can be pointed out from the UV−vis spectra that for ZnO−SnO_2 (SZ) (Figure 2c) and for ZnO−CuO (CZ) (Figure 2b), there is a significant decrease in intensity of the absorption band. This could occur due to the fact that SnO_2 and CuO are the dominant phases over the ZnO in SZ and CZ, respectively. This also can be verified from the energy-dispersive system (EDS) results (Figure S1). The energy band gap values (E_g) were calculated for all the samples and found to be around 3.25, 2.15,, 1.98, and 3.12 eV for Z, CZ, AZ, and SZ, respectively (Figure S2). This variation in E_g could be responsible for the electronic transition that occurs during the interaction between NPs with microorganisms and differentiated their killing efficiency, which has been discussed in details in the subsequent section (see Figure 10).

Furthermore, to check the chemical functionality, the Fourier transform infrared (FTIR) experiments were performed for all the samples. The FTIR of the materials is shown in Figure S5. The stretching bands observed at around 3500 cm^{-1} and at around 1300 cm^{-1} are due to the presence of the O−H bonds. The stretching bands appeared at around 457, 452, 500, and 719 cm^{-1} are due to the Zn−O bond, Cu−O bond, Ag−O, and O−Sn−O bond, respectively.

The solid-state crystal structures and phases of the synthesized materials have been examined through the powder XRD patterns (Figure 3). XRD results of ZnO NPs (Figure 3a) are matching well with the previous report corresponding to the hexagonal Wurtzite phase of the ZnO NPs (JCPDS data card 89-0510). The peaks at 2θ = 32.1, 33.1, 36.3, 45.1, 57.9, 68.8, 70.6, and 77.1° correspond to the (100), (002), (101), (102), (110), (201), (004), and (202) diffraction planes, respectively. The XRD pattern of ZnO−CuO NPs has been shown in Figure 3b, and the diffraction peaks appeared at 2θ ∼

https://doi.org/10.1021/acsomega.1c04139
ACS Omega 2021, 6, 31615−31631

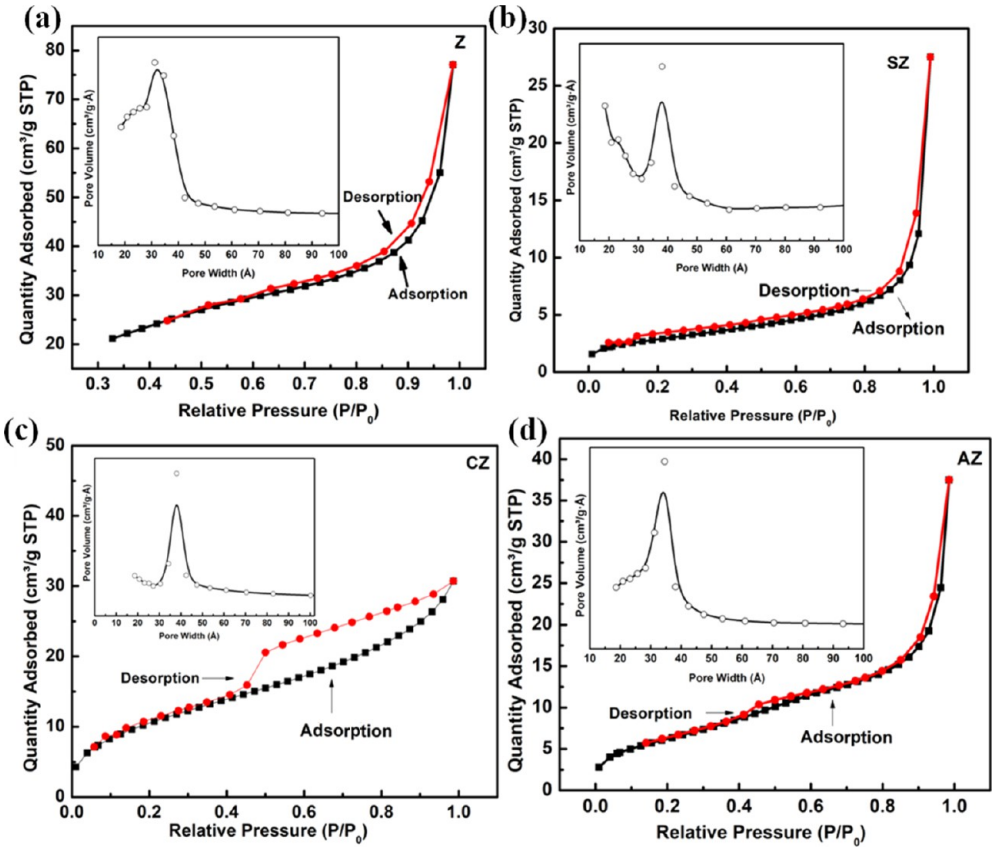

Figure 4. BET surface area analysis results: N_2-adsorption−desorption isotherm plots of (a) ZnO (Z); (b) ZnO−SnO_2 (SZ); (c) ZnO−CuO (CZ); and (d) ZnO−Ag_2O/Ag (AZ). Inset represents the pore size distribution results calculated from the BJH desorption pore volume data for the respective sample.

34.4 and 34.9° correspond to the (100) and (002) planes of the ZnO Wurtzite hexagonal phase, respectively. Furthermore, the peaks appeared at $2\theta \sim 36.7$, 53.2, and 74.3° correspond to the (111), (020), and (004) planes, respectively, for the monoclinic crystalline phase of CuO (JCPDS file number 48-1548).[43] A trace amount of cubic Cu_2O is also present in the composite system (Figure 3b). Figure 3c shows the XRD pattern for ZnO−SnO_2, which is matching well with the previous report.[44] The peaks appeared at $2\theta \sim 30.8$ and 34.5° correspond to the hexagonal phase of ZnO with (100) and (101) diffraction planes, respectively. However, the peaks appeared at $2\theta \sim 32.1$, 42.7, and 62.7° correspond to the tetragonal crystalline phase of SnO_2 with (101), (120), and (310) planes, respectively. Furthermore, it can be seen from Figure 3c that the peaks appeared at $2\theta \sim 80.17°$ correspond to the (400) planes of SnO_2 and (014) of ZnO which co-existed. Furthermore, a trace amount of SnO_2 (200) is also found. Additionally, Figure 3d depicts the XRD peaks for ZnO−Ag_2O/Ag which consists of the cubic phase of ZnO and the cubic phase of Ag_2O, as found out from the Match software pdf no. 16-153-7876 and 96-101-0605, respectively. The diffraction peaks appeared at $2\theta \sim 32.5$, 38.2, 54.8, and 74.5° resemble the (111), (020), (202), and (231) diffraction planes, respectively, that correspond to the cubic phase of Ag_2O. The peaks appeared at $2\theta \sim 33.5$, 56.3, and 67.4° are typically for the cubic ZnO phase belonging to the (111), (202), and (311) planes, respectively. Furthermore, from XRD, it is confirmed that the composite (*i.e.*, ZnO−Ag_2O/Ag) consists of metallic Ag, and the corresponding diffraction peaks appeared at $2\theta \sim 28$, 38.2, 42.5, and 77° for (220), (111), (200), and (311) diffraction planes, respectively. Therefore, the obtained results prove that there are significant diffraction peaks present as the evidence for the presence of AgO_2/Ag^0, SnO_2, and CuO in the final composition. Notably, there is no significant diffraction peaks observed that could be due to the lattice site substitution of ZnO or for the other elements.[45] In conclusion, the XRD results showed that the NP combination system comprises elemental Ag_2O/Ag^0, CuO, and SnO_2 in different combinations with ZnO, and the NP systems are crystalline in nature. These results are further matching well with the transmission electron microscopy (TEM) results (fringes are visible in Figure 1). Elemental analysis results are also matching well with the results obtained from the EDS (Figure S1) and X-ray photoelectron spectroscopy (XPS) experiments (Figure S6). The EDS results, as shown in Figure S1, are also the evidence for the presence of elemental Zn and O in ZnO; Cu, Zn, and O in ZnO−CuO; Ag, Zn, and O in ZnO−Ag_2O/Ag, and Sn, Zn, and O in ZnO−SnO_2.

To find out the physical properties such as surface area and porosity, Brunauer−Emmett−Teller (BET) surface area analysis has been conducted for all the samples, and surface areas were calculated to be 61.0, 40.1, 23.4, and 10.3 m^2/g for the samples ZnO, ZnO−CuO, ZnO−Ag_2O/Ag, and ZnO−SnO_2, respectively. Furthermore, all the samples prepared for this work are found to be porous in nature. The Barrett−Joyner−Halenda (BJH) average pore size is found to be 3−4 nm for all the samples (see inset of Figure 4). The porous nature of the samples is further confirmed through the BJH

https://doi.org/10.1021/acsomega.1c04139
ACS Omega 2021, 6, 31615−31631

isotherm (adsorption−desorption), which is of the type IV category (Figure 4), and the average pore size range shows that the materials are mesoporous in nature which is matching well with the porosity results obtained from the HRTEM images. It is noticed that the specific surface area has decreased in mixed oxide NPs compared to the ZnO NPs which might be due to the blocking of many micropores due to the presence of the tiny metal oxide NPs.[46] Furthermore, the surface area of the ZnO−CuO decreases with increase in the average pore size. The reason behind this phenomenon is that the crystallinity/particle size is inversely proportional to the surface area, and XRD shows that the ZnO−CuO (Figure 3b) is quite amorphous in nature due to the smaller particle size. It can be further noted that the porous structure and the particle size strongly influence the antimicrobial properties due to the change in the surface area and the availability of active sites of interactions with them.

The thermal stability of the samples was investigated through thermogravimetric analysis (TGA) analysis (Figure S3). Results showed that the weight loss for all the samples occurred in the temperature range of 40 °C ≤ T ≤ 200 °C due to the evaporation of unbound moisture present in the samples. The weight loss continues up to 619 °C for ZnO, 848 °C for ZnO−CuO, 745 °C for ZnO−SnO_2, and 459 °C for ZnO−Ag_2O/Ag until they become stable. The weight loss at the higher temperature occurred due to the creation of oxygen vacancy in ZnO. From the above results, we also noticed that for ZnO−Ag_2O/Ag, a sharp decline or intense exothermic peak was observed at ∼800 °C [in differential scanning calorimetry (DSC) results, Figure S4] which attributed to the recrystallization of the NPs[47] and found stable between 459 °C ≥ T ≤ 800 °C. However, the obtained results describe that the mixed oxides are more stable than the single oxide (ZnO). From Figure S4d, we observed that there is a slight dip in the endothermic peak at ∼438 °C, and this occurred due to the release (evaporation) of Zn metal (the melting point of pure Zn is around 420 °C). From Figure S4, it is also clearly noticed that there is no substantial change in the thermo gram. However, one endothermic peak at 190 °C for Z (ZnO) and AZ (ZnO−Ag_2O/Ag) is observed, which may be due to the loss of moisture (from Zn−OH) (see the FTIR spectra also, Figure S5).

To check the colloidal stability of the NPs, the surface charge potential was measured through the surface charge zeta potential (ς) measurement of the samples without any surface modification or adding surfactant, and the ς values varied in the order of ZnO−SnO_2 < ZnO−Ag_2O/Ag < ZnO−CuO < ZnO. Result shows that the ς values are in a broad range, and colloidal stability varied on the types of particles,[48] and the NPs are suitable for the biological applications.[49] Furthermore, the stability of the composite NPs was investigated in phosphate buffer (PB), phosphate-buffered saline (PBS) (pH, 5, 6.9, 7.4, and 8), and saline solutions over a period of 7 days with keeping the fixed concentration of the samples. The obtained results have been tabulated in Tables S1−S4. From Table S1, it is clearly observed that zeta potential values for ZnO (Z) in PBS of (1) pH 5 varied in between −12.0 and −10.9 mV over a time period of 7 days; (2) for pH 6.9, potential values varied in between −15.3 and −20 mV; for pH 7.4, potential values varied in between −15.5 and −16.1 mV, and for (4) pH 8, the potential values varied from −23.4 to −30 mV. However, for longer period of time, the potential values decreased within the time period of 2−7 days. Zeta potential values for the ZnO−Ag_2O/Ag (AZ) sample were measured in PBS, and the values are tabulated in Table S3 over a time period of 7 days, and the values obtained to be (i) −10.9 to −12.3 mV (for pH 5), (ii) −14.2 to −20.8 mV (for pH 6.9); (iii) −16.2 to −10.1 mV (for pH 7.4); and (iv) −1.9 to −4.1 mV (for pH 8), respectively. Till the time period of 7th day and at higher pH (pH 8), the sample becomes unstable in PBS. In Table S2, the zeta potential values for all the samples in saline solution have been shown, and it was found that all the samples are stable at least up to 2 days. However, over the time period of 7 days, their zeta potential values were decreased. Zeta potential for all the samples in PB Solution have been investigated (see Table S4) and found that ZnO−Ag_2O/Ag (AZ) are quite stable in the physiological pH 6.9 and pH 7.4. All the other samples are found to be stable in PB at different pH values. In conclusion, all samplers are stable in saline solution up to 48 h, and ZnO−Ag_2O/Ag (AZ) is very stable among all the samples. Details of zeta potential values are tabulated in Tables S1−S4.

Time-scale dissolution studies for all the samples were conducted through DLS for 7 days, using saline, PBS, and PB solutions of different pH 5, 6.9, 7.4, and 8, and the results are represented in Tables S5−S11. It is clearly evident that the hydrodynamic diameters of the particles varied in saline, PBS, and PB. The hydrodynamic diameters have been calculated for all the samples dispersed in PBS, and it shows that particle size of ZnO−Ag_2O/Ag (Table S6) is found to be quite stable, whereas for ZnO, it was fluctuating (Table S5) at different pH values, 5, 6.9, 7.4, and 8. In saline solution, all the types of NPs are quite stable at least for 7 days, and the stability is found more for ZnO−Ag_2O/Ag with respect to the other samples, such as ZnO, ZnO−CuO, and ZnO−SnO_2 (Table S7). For ZnO, ZnO−CuO, and ZnO−SnO_2, the increase in hydrodynamic diameters is observed, which may be due to the settlement of the particles or due to their coagulation.

Furthermore, hydrodynamic diameters of all the types of particle in PB solution of different pH values (5, 6.9, 7.4, and 8) have been evaluated. The more fluctuation of the size has been observed for ZnO for different pH values in the entire time period (Table S8), while for ZnO−Ag_2O/Ag, the variation of the particle size is found to be in the considerable range (see Table S9). A similar phenomenon was observed for ZnO−CuO (Table S10) and ZnO−SnO_2 (Table S11) at different pH values and time periods. As per our analysis, this variation of size observed may be due to the change in the pH which has further affected the dissolution of particles as we observed the change in color of the solution. Under acidic conditions, the NPs may be agglomerated in the faster rate, and it is also observed that the rate of agglomeration varied for the different samples. However, we should not compare the particle size results obtained from TEM and DLS since DLS samples were dispersed in different solutions (saline, PB, and PBS) for up to 7 days at different pH values, whereas the TEM/HRTEM experiments were performed by dispersing the samples in dry propanol followed by drying on TEM grids (Formvar/C coated Cu grid, mesh size 200). Therefore, from the time-scale zeta potential and dissolution studies, it can be concluded that the mixed oxide NPs prepared for this work are more stable compared to the ZnO alone, and good bioavailability can be achieved during any biological and antimicrobial applications.[48]

XPS analysis was performed for the determination of the elemental composition of the samples, and Figure S6 shows the

https://doi.org/10.1021/acsomega.1c04139
ACS Omega 2021, 6, 31615−31631

Table 1. Binding Energy (kcal mol^{-1}) and Interaction Parameters of NPs with Interacting Proteins Calculated from an *In Silico* Study[a]

Sr. no	organism name protein/pubmed ID	ligand NPs	binding energy (kcal/mol)	inhibition constant	hydrogen bond/amino acid residue	amino acid interaction
		Ag	−1.64	63.28 mM		SER205, GLN203, HIS204, **LEU208**, ASP150, ASP131, SER199, SER201
		SnO_2	−3.92	1.33 mM	ILE155 (1.766 Å)	LYS154, ILE155, GLN160,TYR270,
		ZnO	−5.61	77.18 μM	**GLN194** (2.085 Å)	VAL211, PRO210, **GLN194**, ARG209, **LEU208**, **LEU197**, **ILE236**,**LEU197**
					LEU197 (1.922 Å)	
1	*P. aeruginosa* PqsR (MvfR) PDB ID-**4JVI**	CUO	−7.50	3.17 μM	**ILE236** (2.173 Å)	
					LEU197 (1.931 Å)	GLN195, **LEU208**,**LEU197**, **SER196**, **PHE221**, **MET224**, **ILE236**
		ZnO−CuO	−9.03	241.04 nM	**ILE236** (1.875 Å)	
					LEU197 (2.248 Å)	GLN194, **LEU208**, SER196, LEU197 **ILE236**, ILE149, ALA168, ALA237, **PHE221**
		$ZnO-SnO_2$	−9.07	224.6 nM		ILE186, LEU189, **VAL211**, TRP234, TYR258, **ILE236**
		$ZnO-Ag_2O/Ag$	−9.79	66.48 nM	SER106 (2.099 Å)	TYR240, SER106, GLY296, HIS239, **LYS167**, THR166, PRO104
					TYR240 (2.096 Å)	
2	*A. baumannii* **RstA PDB ID-5E3J**	Ag	−1.73	53.94 mM		THR23, ALA20, ILE12, VAL56,VAL13, GLU14, ASP58, LEU84
		SnO_2	−3.90	1.39 mM		ILE12, VAL56
		ZnO	−4.83	289.86 μM	ALA106 (1.905 Å)	**ARG117**, VAL105, ALA106,**GLN93**, **TYR104**
					ARG117 (2.162 Å)	
					GLN93 (2.106 Å)	
					ALA106 (2.143 Å)	
		CuO	−5.33	123.94 μM	ARG124 (2.207 Å)	**HIS78**, ARG123, **ARG124**, GLY100, ARG74
					HIS78 (2.151 Å)	
		ZnO−CuO	−7.50	3.18 μM	ARG117 (2.096 Å)	VAL104, ALA106, VAL109, **GLN93**, **ARG117**, **VAL113**, GLN110
					GLN93 (1.873 Å)	
		$ZnO-SnO_2$	−10.72	13.94 nM	GLN93 (1.754 Å)	**VAL113**, GLN93, **TYR104**, **ARG117**, VAL105, ALA106 TYR104
					ALA106 (2.022 Å)	
		$ZnO-Ag_2O/Ag$	−12.0	1.61 nM	ALA106 (2.034 Å)	VAL105, VAL109, **VAL113**, ALA106, LYS107, **GLN93**, **ARG117**, **TYR104**, GLN110, ALA106
					GLN110 (2.207 Å)	
					ALA106 (1.893 Å)	
3	*K. pneumoniae*/ FosA PDB ID-5WEW	Ag	−1.48	82.78 mM		LEU114, ILE72, PHE70, SER71, MET28, CYS42
		SnO_2	−3.60	2.31 mM	LYS111 (1.914 Å)	LYS111, THR66, HIS110
		ZnO	−5.17	163.38 μM	ARG55 (1.830 Å)	ARG55, GLY109, THR58, LYS111, THR66, ASP64, SER63
					THR58 (2.232 Å)	
					SER63 (1.626 Å)	
					LYS111 (1.761 Å)	
		CUO	−3.21	4.43 mM	TYR131 (2.209 Å)	ARG96, GLN129, **TYR131**, GLN129
		ZnO−CuO	−7.44	3.54 μM	SER63 (1.661 Å)	SER63, LYS111, ARG55, GLY109, HIS110, THR66, TYR68
					LYS111 (1.839 Å)	
		$ZnO-SnO_2$	−8.04	1.28 μM	ASP64 (1.948 Å)	SER63, THR58, ARG55, TYR68, HIS110, THR58, ASP64
					HIS110 (2.238 Å)	
		$ZnO-Ag_2O/Ag$	−11.57	3.33 nM	LEU119 (1.852 Å)	LEU119, SER118, **HIS115**, GLY117,VAL116, ILE72, SER71, GLU74, GLN121
					GLN121 (2.119 Å)	
4	*C. albicans* Hsp90 PDB ID-**6CJP**	Ag	−1.63	63.89 mM		LEU176, **ASN40**, **THR174**, ILE80, **ASP82**, ALA41, ARG81, ILE67
		SnO_2	−4.14	926.71 μM	ILE99 (2.024 Å)	ILE99
		ZnO	−4.97	227.87 μM	GLN5 (2.049 Å)	THR98, ILE99, ILE15, THR12, GLN5, PHE4
					ILE99 (2.046 Å)	

https://doi.org/10.1021/acsomega.1c04139
ACS Omega 2021, 6, 31615−31631

Table 1. continued

Sr. no	organism name protein/pubmed ID	ligand NPs	binding energy (kcal/mol)	inhibition constant	hydrogen bond/amino acid residue	amino acid interaction
		CuO	−5.72	64.22 μM	LYS47 (2.174 Å)	**MET87**, **ASN40**, GLY86, **LYS47**, ILE85, **ALA44**
					GLY86 (1.920 Å)	
		ZnO−CuO	−8.61	486.66 nM	GLN5 (2.194 Å)	ALA13, GLY157, **PHE159**, **HIS9**, THR12, SER16, GLN5, ILE15, PHE4, GLY97, ILE99
					ILE99 (1.825 Å)	
		$ZnO-SnO_2$	−9.31	149.24 nM	ASN95 (2.220 Å)	**PHE127**, THR98, **GLY126**, GLY124, **ASN40**, ASN95
					GLY126 (2.148 Å)	
		$ZnO-Ag_2O/Ag$	−11.32	5.06 nM	THR12 (2.018 Å)	LYS158, **THR160**, **PHE159**, VAL161, ALA13, **HIS9**, THR12, GLU10, VAL93, LYS89, GLU7, THR8
					LYS89 (2.055 Å)	

[a]It can be noted that the bold residues represent active binding sites interacted with inhibitors reported on PDB and earlier publications.

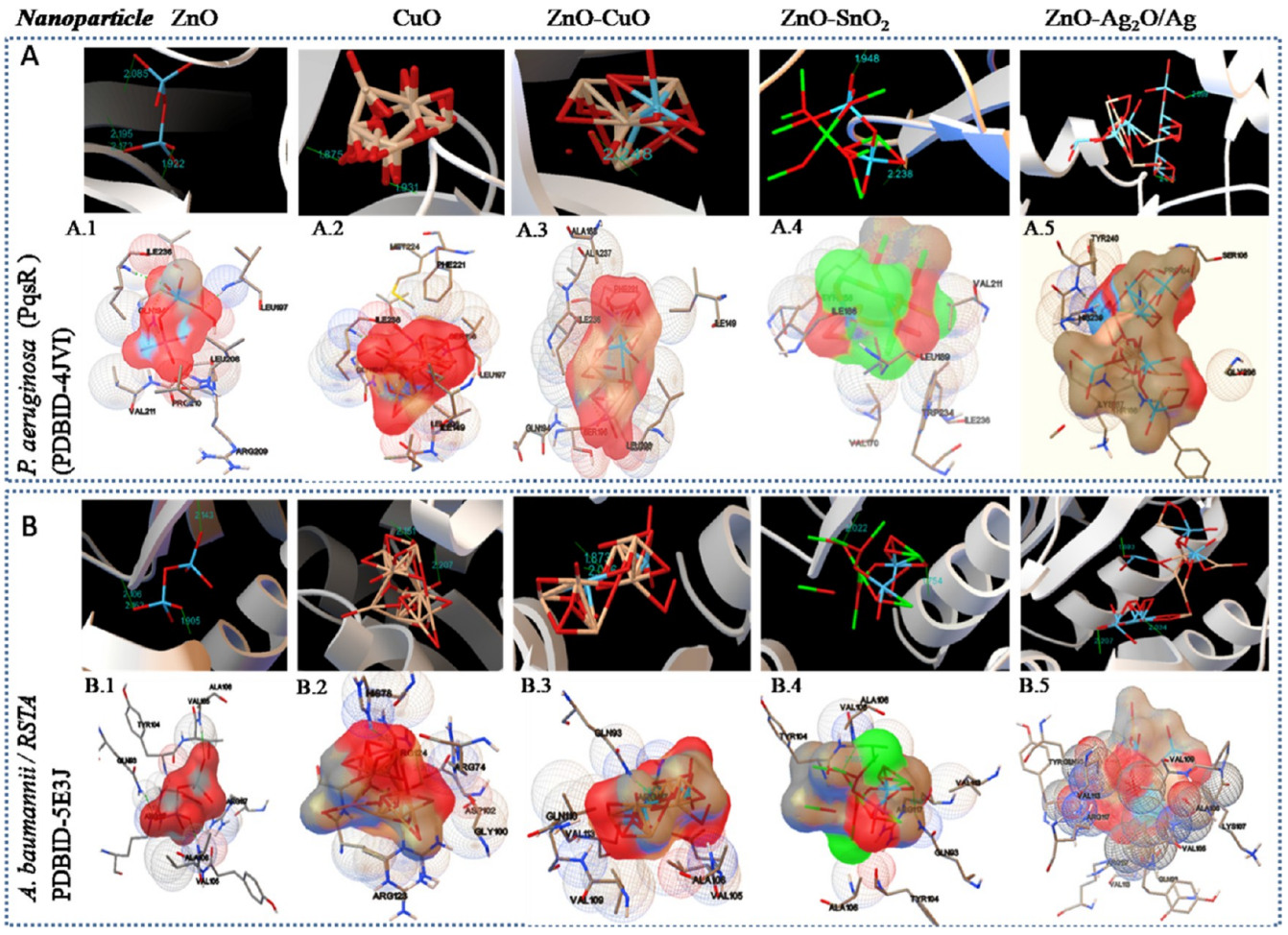

Figure 5. Molecular interactions of bacterial/fungal proteins with NPs. (A,B) Crystal structure of PqsR and RstA (BmfR) (ribbon structure), respectively. (A.1−A.5) (Upward) Showed PqsR interactions and hydrogen bonding (green thin line with distance) with ligands ZnO (Zn-blue), CuO (Cu-peach), ZnO−CuO, $ZnO-SnO_2$ (Sn-lime green), and $ZnO-Ag_2O$ (Ag-coral), respectively. (B.1−B.5) Crystal structure BmfR interacted with ligands such as ZnO (Zn-blue), CuO (Cu-peach), ZnO−CuO, $ZnO-SnO_2$ (Sn-lime green), and $ZnO-Ag_2O$ (Ag-coral), respectively. Downward figures represent the interacting residues of amino acids of active pocket and oxygen molecules (red).

XPS spectra of the mixed oxide composites, in which Figure S6a−c represents the spectra of ZnO−CuO; Figure S6d−f of $ZnO-SnO_2$; and Figure S6g−i of $ZnO-Ag_2O/Ag$. The appeared band at ∼530 eV signifies the presence of oxygen (O 1s) in each nanocomposite. As shown in Figure S6a, the bands appeared at the energy level 933.4, 77, 1020.3, and 1043.3 eV correspond to the binding energies for Cu $2p_{3/2}$, Cu $3p_{3/2}$, Zn $2p_{3/2}$, and Zn $2p_{1/2}$, respectively.[50] Furthermore, a minor shift in the binding energy band of Zn and splitting energy bands (∼23 eV) between Zn $2p_{1/2}$ and Zn $3p_{3/2}$ indicate the strong interactions that occurred between the CuO and ZnO due to the local difference in the atomic

https://doi.org/10.1021/acsomega.1c04139
ACS Omega 2021, 6, 31615−31631

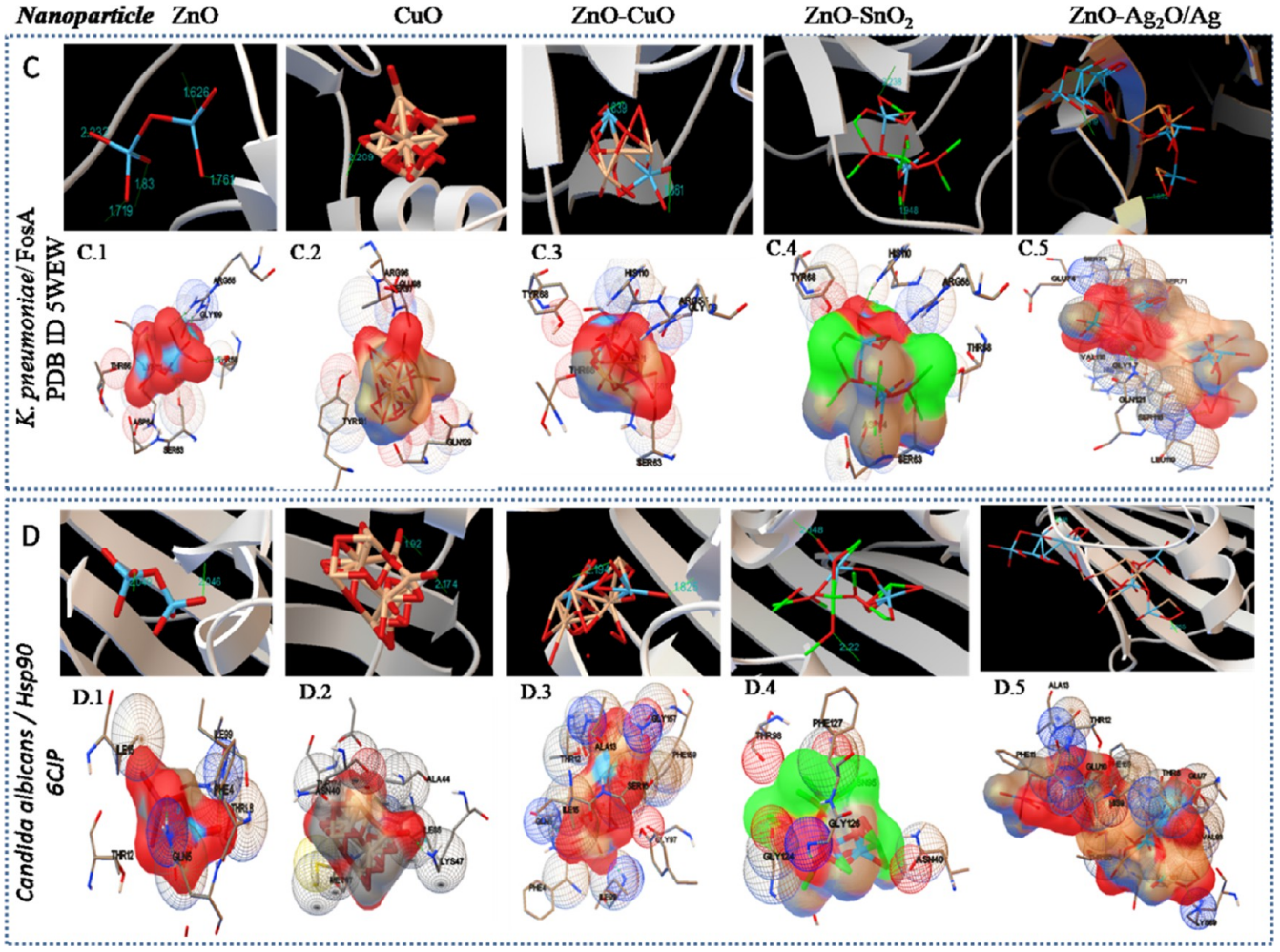

Figure 6. Molecular interactions of bacterial/fungal proteins with NPs. (C,D) Crystal structures of FosA and Hsp90 (ribbon structure), respectively. (C.1−C.5) (Upward) Shows FosA interactions and hydrogen bonding (green thin line with distance) with ligands ZnO (Zn-blue), CuO (Cu-peach), ZnO−CuO, ZnO−SnO_2 (Sn-lime green), and ZnO−Ag_2O (Ag-Coral), respectively. (D.1−D.5) Crystal structure Hsp90 interacted with ligands ZnO (Zn-blue), CuO (Cu-peach), ZnO−CuO, ZnO−SnO_2 (Sn-lime green), ZnO−Ag_2O (Ag-Coral), and oxygen (red), respectively. Downward figures represent the interacting residues of amino acids of active pocket with NPs.

environment.[51] Figure S6c represents the bands for Cu $2p_{3/2}$ of ZnO−CuO, which can be deconvoluted into three energy bands, and it confirms for the presence of three oxidation states of the elemental copper, that is, Cu^{+2}, Cu^{+1}, and Cu^0 in the composite system. The formation of Cu^0 (copper zero) subsequently translated into Cu_2O (Cu^{+1}) and CuO (Cu^{+2}) due to the use of the strong reducing agent $NaBH_4$ and as the entire reaction has been performed in the oxygen environment. Figure S6b shows the XPS spectra for Zn $2p_{3/2}$ and the binding energy bands observed at ∼1021.70 and ∼1020 eV, which are the characteristics bands for the ZnO. From the full range of the XPS spectrum of ZnO−Ag_2O/Ag (as shown in Figure S6g), it is identified that the energy bands appeared at 87, 576, 1020.2, and 1043.2 eV correspond to the presence of Zn $3p_{3/2}$, Ag $3p_{3/2}$, Zn $2p_{3/2}$, and Zn $2p_{1/2}$ states, respectively. Figure S6g has been expanded into the region between 520 and 600 eV (represented in the inset), which supports for the presence of O 1s and Ag $3p_{3/2}$. Figure S6i shows the XPS energy band for Ag 3d, and Figure S6h shows for Zn $2p_{3/2}$ present in ZnO−Ag_2O/Ag, which further shows that the presence of Ag_2O corresponds to the band appeared at ∼367.6 eV. Interestingly, Figure S6h also shows the presence of Ag (∼371.9 eV) and AgO (367.4 eV) in ZnO−Ag_2O/Ag.[52,53] This means that Ag_2O was formed during the reduction reaction, and the same was transformed into the Ag^0. Figure S6h shows the Zn $2p_{3/2}$ peak at 1020.2 eV, which is matching well with the previously reported results. For XPS spectra of ZnO−SnO_2, bands for Zn 2p and Sn 3d are depicted in Figure S6d−f, respectively. The bands appeared at 88, 139.9, 485, 494, 715, 757, 884.8, 1020, and 1043 eV correspond to the presence of Zn $3p_{3/2}$, Sn 4s, Sn $3d_{5/2}$, Sn $3d_{3/2}$, Sn $3p_{3/2}$, Sn $3p_{5/2}$, Sn 3s, Zn $2p_{3/2}$, and Zn $2p_{1/2}$, respectively. The band observed at 25.1 eV is a characteristic peak for the Sn 4d (Sn^{+2}) state, which suggests that it indeed formed SnO_2 NPs.[54] It is also evident for the presence of Sn and SnO which has been confirmed from XRD results (Figure 3c). The binding energy of elemental oxygen at 530 eV also suggests that it appeared due to the presence of metal oxide.[54,55] The minor peak shifting for Sn 3d is observed, which might be due to the chemical modification and lattice interactions between the elemental Zn and Sn, which further has been supported by the TEM results (Figure 1c). All these results are interesting for its use as an antimicrobial component, which has been explained in the subsequent section.

Then, the *in silico* computational approach was taken into consideration to determine the bactericidal/fungicidal activities

https://doi.org/10.1021/acsomega.1c04139
ACS Omega 2021, 6, 31615−31631

of bimetallic composite NPs compared to the single metal oxide NPs. Molecular interaction between NP with quorum-sensing regulator PqsR (PDB ID: 4JVI), response regulator RstA(PDB ID: 5E3J), fosfomycin resistance protein (PDB ID: 5WEW), and heat shock protein 90 (PDB ID: 6CJP) has been analyzed. The binding energy and affinity, inhibitory constant, interacting polar bonds, and interacted amino acids for the single metallic/oxide and bimetallic/oxide NPs have been represented in Table 1 and Figures 5 and 6. For single metallic/oxide NPs, a highest binding energy affinity was observed when CuO NPs interacted with the PqsRA, RstA, and Hsp90, and the values are −7.50, −5.33, and −5.72 (kcal/mol), respectively, while ZnO NPs interacted with the FosA with a required binding energy affinity of −5.17 kcal/mol (see Table 1). It is further observed that a very low binding energy for Ag and SnO_2 NPs was required, while ZnO NPs were required almost in an equivalent amount of binding energy for PqsR, RstA, FosA, and Hsp90, such as −5.61, −4.83, −5.17, and −4.97 kcal/mol, respectively. It is also found out that the higher polar interactions played with ZnO NP along with all the listed proteins. Therefore, combination of ZnO−CuO, ZnO−SnO_2, and ZnO−Ag_2O/Ag has been chosen for further protein−ligand interactions analysis (ribbon structure, as shown in Figures 5 and 6), and hydrogen bond (with thin green line) polar and nonpolar interactive amino acids (spherical) have been represented in Figures 5 and 6. Inhibition constants are calculated for the interactions between ZnO with PqsR, RstA, FosA, and Hsp90, which are as follows: 77.18, 289.86, 163.38, and 227.87 μM, respectively. CuO NPs also interacted with the PqsR, RstA, FosA, and Hsp90, and the interaction constants obtained to be 3.17, 123.94, 4.43, and 64.22 μM, respectively. While for all the bimetallic/oxide NPs, during the interaction with PqsR, RstA, FosA, and Hsp90, the inhibition constants decreased to nanomole with increase in the binding energy affinity. Among these three NP systems, such as ZnO−CuO, ZnO−SnO_2, and ZnO−Ag_2O/Ag, the highest binding energy affinity was observed for ZnO−Ag_2O/Ag, while it was interacting with the PqsR, RstA, FosA, and Hsp90, and the values calculated to be −9.79, −12.0, −11.57, and −11.32 (kcal/mol), with minimum inhibition constants of 66.48, 1.61, 3.33, and 5.06 nM, respectively. It is also noticed that ZnO−CuO, ZnO−SnO_2, and ZnO−Ag_2O/Ag NPs possessed excellent antimicrobial and antifungal activities with higher efficiencies compared to the single metal or metal oxide NPs. However, among these NPs, the ZnO−Ag_2O/Ag NPs exhibited highest antimicrobial efficacy compared to the other samples used. It can also be noticed that the presence of octahedral and cubic phase of Cu_2O can affect the antibacterial activity;[56] however, the extent of Cu_2O present in our composite system is very less/negligible.

Furthermore, the intermolecular interacting amino acids and the hydrogen bonding resulted with ZnO, CuO, ZnO−CuO, ZnO−SnO_2, and ZnO−Ag_2O/Ag are shown in Figures 5 and 6 and for *P. aeruginosa* (Figure 5A), *A. baumannii* (Figure 5B), *K. pneumoniae* (Figure 5C), and *C. albicans* (Figure 5D), respectively. *P. aeruginosa* (Gram-negative) bacterium is a causative agent of the nosocomial infection. A virulence factor PqsR involved in the pathogenicity belongs to the family of the LysR-type transcriptional regulator. The active motif of PqsR can be interacted with the various inhibitors such as (i) quinolone derivative interacting amino acids including Asn206-(H), Arg209(H), Leu197(H), Glu259(H), Phe221, Leu207-(H), and Ser196,[57] (ii) stigmatellin Y interacting amino acids including Pro129, Ala187, Ala190, and Val211,[58] and (iii) zingerone interacting amino acids including Leu208(H), Gln194(H), Met 224, Ile236, Leu207, Val211, Pro210, Arg209, and Ser196.[59] From our study, it is observed that except ZnO−Ag_2O/Ag, other NPs (Figure 5A.1−A.4) interacted with the active motif of PqsR (represented in bold in Table 1), and it showed the anti-biofilm activity. ZnO forms the hydrogen bonding with the Gln194, Leu19, and Ile236 and with other intermolecular interactions with Val211, Pro210, Arg209, and Leu208 (Figure 5A.1). It shows that the ZnO−Ag_2O/Ag NPs interact at different motifs with higher affinity forming the hydrogen bonds with Tyr240, Ser106, and other interacting nonpolar interaction proteins including Gly296, His239, Lys167, Thr166, and Pro104 (Figure 5A.5).

RstA(BfmR) is a master regulator of biofilm initiation in *A. baumannii* which is regulated by the csu operon and increased the resistance toward the erythromycin, colistin, imipenem, and rifampin. The csu operon was involved in the attachment of biofilms to abiotic surfaces both in nature and in the clinic. Molecular dynamic stimulation showed that the α4-β5-α5 segment of BfmR is an active motif.[60] The crystal structure of BfmR is an active homodimer conformation consisting of two active residues such as Thr85 and Tyr104. Previous studies showed strong binding hot spot residues including Arg124 and His78, while Glu98, Arg112, and Arg119; Asp102 and Arg124; and Asp103 and Arg117 residues were involved in the salt bridge formation.[60,61] As represented in Figure 5B.1−B.5 and Table 1, our *in silico* studies showed that the ZnO, CuO, ZnO−CuO, ZnO−SnO_2, and ZnO− Ag_2O/Ag NPs interacted at an active site of BfmR, and it is represented in bold. The highest binding interaction of 5E3J with ZnO−Ag_2O and ZnO−SnO_2 is observed with energy −12.0 (kcal/mol) by forming hydrogen bonds with the residues Ala106 and Gln110 with an energy value −10.72 (kcal/mol). The hydrogen bonds formed with the residues Ala106 and Gln93, as shown in Figure 5B.3,B.5. Active binding of ZnO with Arg117, Gln93 and TYR 104 of 5E3J, CuO with His78 and Arg124, ZnO−CuO with Gln 93 and Val113, ZnO−SnO_2 with Val113, Gln93, Tyr104, and Arg117, and ZnO−Ag_2O/Ag with Val113, Gln93, Arg117, and Tyr104 has shown inhibition of Bmfr. Arg111 and Arg118 of Phop of *E. coli* are analogous to bfmRArg117 and BfmR Arg124 which possessed strong hot spots for binding.[61]

Expanded clinical usages of fosfomycine result in the development of fosfomycine-resistant *K. pneumoniae* strain. Fosfomycine shows a bactericidal effect only when the fosA gene is deleted. Investigation of the FosA inhibitor will help overcoming from multidrug resistance.[37] An important interacting residue of FosA includes β2-β3 from residues 31 to 46 and β6-α3 helix residue from 115 to 135. The interactions with 5WEW between NPs such as ZnO, CuO, ZnO−CuO, ZnO−SnO_2, and ZnO−Ag_2O/Ag have been shown in Figure 6C.1−C.5. Polar interactions formed between (i) CuO with Tyr131; (ii) ZnO with Arg55, Thr58, Ser63, and Lys111; (iii) ZnO−CuO with Ser63 and Lys111, (iv) ZnO−SnO_2 with Asp64 and His110, and (v) ZnO−Ag_2O with leu119 and Gln121 with highest binding affinity −11.57 (kcal/mol). Other interacting amino acids are represented in Table 1, and Figures 5 and 6 can also interact.

Furthermore, molecular chaperone Hsp90 governs the key function of morphogenesis, and inhibition of Hsp90 alters the capsule assembly and virulence property of pathogen. Co-crystal structure of Hsp90 nuclear-binding domain of *C.*

https://doi.org/10.1021/acsomega.1c04139
ACS Omega 2021, 6, 31615−31631

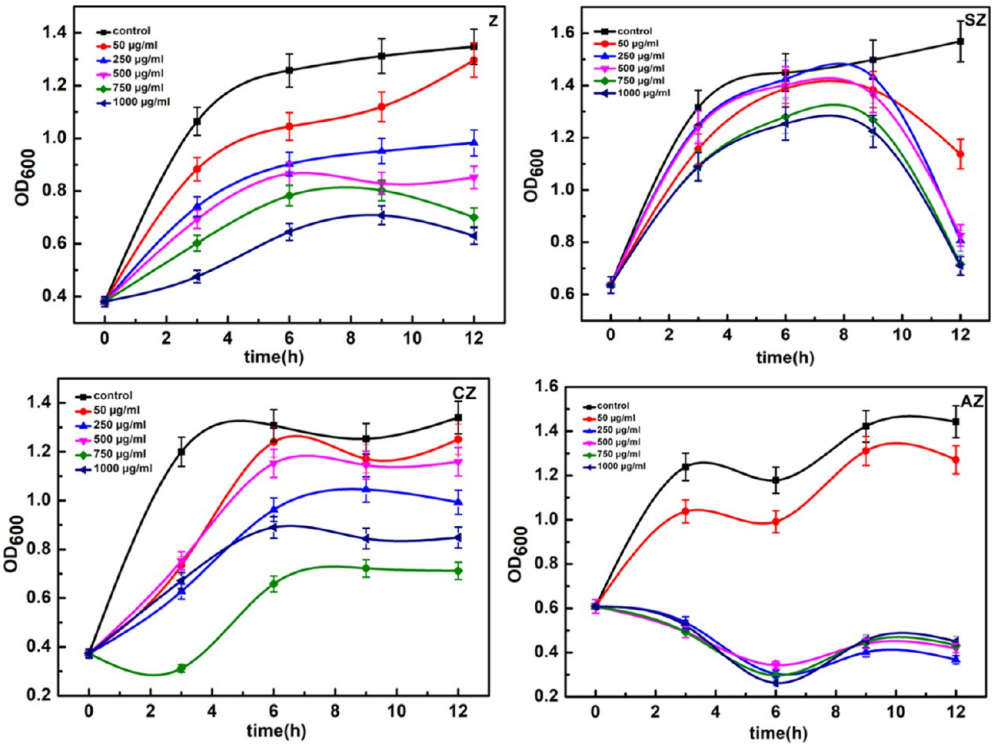

Figure 7. Antibacterial activity results of (Z) ZnO, SZ (ZnO−SnO_2), CZ (ZnO−CuO), and AZ (ZnO−AgO_2/Ag) at different time intervals with *E. coli*.

albicans with CMLD013075 showed the unique target-specific structural rearrangement.[62] Hsp90 inhibitor showed antifungal activity when it bound to the ATPase domain forming residues 29−184.[62,63] Single or bimetallic oxide NPs interacted with ATPase domain residues, as shown in Figure 6D.1−D.5. Polar interactions occurred for (i) CuO with Lys47 and Gly86; (ii) ZnO with Gln5 and Ile99, (iii) ZnO−CuO with Gln5 and Ile99, (iv) ZnO−SnO_2 with Asn95 and Gly126, and (v) ZnO−Ag_2O/Ag with Thr12 and Lys89. Many interactions observed with other residues are represented in Table 1 and Figure 6. In comparison to ZnO, when ZnO doped with CuO, SnO_2, and Ag_2O, the antibacterial and antifungal properties are found enhanced significantly in many folds. Among these three doped compositions, *in silico* studies conclude that ZnO−Ag_2O/Ag is an effective component having highest antimicrobial properties. Furthermore, we have performed *in vitro* studies for all the components since all are indicating good targeted results.

Finally, the *in vitro* antimicrobial study was conducted against *E. coli,* according to the method as mentioned in the experimental section. The OD_{600} values were calculated with a regular interval of 3 h for up to 12 h for each set of sample and at various concentrations, that is, 0, 50, 250, 500, 750, and 1000 μg/mL.

The antibacterial activity results of different NPs in different concentrations with different time intervals have been shown in Figure 7. All the NPs exhibited regular trends that increase in the concentration from 50 to 1000 μg/mL. The antibacterial activity or rate of inhibition increases after 3 h, and the highly effective results have been obtained at 12 h of incubation. Similar trends were observed for all the NPs such as for ZnO, ZnO−SnO_2, ZnO−AgO_2/Ag, and ZnO−CuO, out of which the ZnO−AgO_2/Ag composite NP system exhibited best antibacterial efficacy. Interestingly, ZnO−AgO_2/Ag NPs exhibited very high antibacterial activities at very low concentration of NPs (50 μg/mL) even at 3 h. For more clarity, bar graph plots are presented in Figure S7, which clearly show that with change in the minimum concentration, a huge change in the antibacterial activity has been obtained.

However, with comparison of all NPs, it can be concluded that the bimetallic mixed oxide composite NPs have exhibited better efficacies than the single one. The ZnO acts as an antibacterial agent by two ways: (i) by ROS generation and (ii) by zinc ions release/diffusion,[5] Similarly, many antimicrobial mechanisms have been proposed using silver nanomaterials.[7] Ag NPs have the ability to penetrate bacterial cell wall through pits formation and release silver ions that inhibit the growth of microorganism. For CuO and SnO_2 NPs, the antibacterial mechanisms have also been discussed, and it has also been narrowed down to ions release and ROS formation, which attack the important cellular components and kill the microorganisms.[6,8] Metallic NPs can also inhibit the growth of the microorganism.[9] Similarly, we can conclude that the present antibacterial materials also follow the ROS mechanism which subsequently has been discussed (Figure 10). However, mixed bimetallic oxides combination with tiny metallic NPs (of size 2−3 nm) accelerated the antimicrobial activities much more through a cooperative electrochemical mechanism, and the band energy gap (E_g) altered and subsequently promoted the ROS formation.

Furthermore, *in vitro* studies were conducted for screening antimicrobial and antifungal activities of synthesized NPs through ZOI studies (Figures 8 and 9), and their efficacy was evaluated through the calculation of MIC. Some nosocomial bacterial strains were selected for this study because these bacteria and fungus can form biofilms on the biomedical implants in hospital quickly and increase the infection levels. Herein, we have calculated the MIC values for all the synthesized mixed metal oxide/metal NPs, and their results

https://doi.org/10.1021/acsomega.1c04139
ACS Omega 2021, 6, 31615−31631

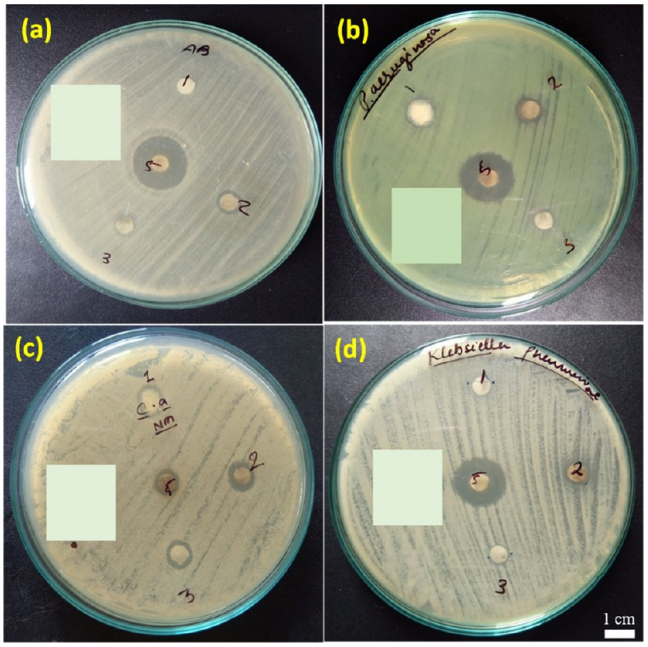

Figure 8. ZOI results obtained for (a) *A. baumannii*, (b) *P. aeruginosa*, (c) *C. albicans*, and (d) *K. pneumoniae*. "1," "2," "3," and "5" labels used for the (Z) ZnO, CZ (ZnO−CuO), SZ (ZnO−SnO_2), and AZ (ZnO−AgO_2/Ag), respectively.

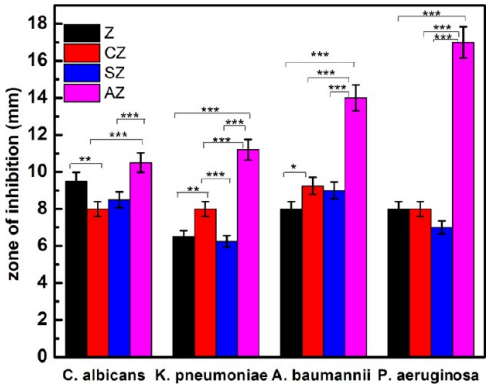

Figure 9. Bar plot representation of ZOI in different strains obtained using different metal oxide composite NPs (*P < 0.05, **P < 0.01, and ***P < 0.001).

were calculated with their single metal oxide NPs keeping the molar equivalent metallic components. Few mixed oxide NPs exhibited excellent MIC results, as shown in Table 2. From Figures 8 and 9, it is clearly evident that the mixed metal oxide composite NPs (ZnO−Ag_2O/Ag) exhibited excitingly a maximum of 17 mm ZOI in *P. aeruginosa*, 11.2 mm in *K. pneumoniae*, 14 mm in *A. baumannii*, and with 10.5 mm inhibition in *C. albicans*. Consequently, ZnO−CuO NPs exhibited ZOI of 9.25 mm in *A. baumannii*, 8.1 mm in *P. aeruginosa*, 8.2 mm in *K. pneumoniae*, and 8 mm inhibition against the *C. albicans*. For ZnO−SnO_2, the ZOI calculated to be 8.5, 6.25, 9, and 7 mm for *C. albicans*, *K. pneumoniae*, *A. baumannii*, and *P. aeruginosa*, respectively. These results were compared with the results obtained for ZnO NPs alone with equivalent molar concentration of metallic Zinc and found the ZOI results obtained to be 8 mm in *P. aeruginosa*, 6.5 mm in *K. pneumoniae*, 8 mm in *A. baumannii*, and 9.5 mm in *C. albicans*. Thus, mixed metal oxide NP system with ZnO exhibited noticeably very high antimicrobial activities compared to the ZnO NPs alone. Thus, it can be concluded that the mixed oxide composite NPs are excellent in preventing bacterial and fungal growth and act as exhibiting better fungicidal and bactericidal activities compared to a single oxide system such as ZnO, CuO, Ag_2O, AgO, or SnO_2. It can only be possible when mixed oxide NPs have the ability to rupture or distort the phospholipid bilayer membrane of bacteria cells with higher penetration rates and with higher electronic interaction in cooperative manner and consequently give excellent results as a whole. Furthermore, mixed oxide NPs can alter or block the ion channels present on the membrane better than a single type of oxide. Additionally, it can be assumed that the tiny mixed oxide NPs (size below 5 nm, about 2−5 nm size) can easily penetrate through the cellular membrane directly with a cooperative understanding which further creates more oxidative stress through participation in physiochemical reactions and disturbs the overall balance of the inter cellular environment and subsequently damages the genetic materials of microorganism and promotes the leakage of internal components of microorganism.[64] Raghunath and Perumal[2] reported that antibacterial properties increased with the decrease in the particle size for single metal oxide NPs. In this line, we can propose that not only the particle size but the electrochemical environment of mixed oxide also has a great role in the killing of microorganisms with better efficacy with creating a unique electrochemical reaction. Furthermore, smaller sized mixed oxide NPs may have more permeability and penetration efficiency compared to the bigger sized particles, which further excel the antibacterial activity or ZOI.[65] Figure 9 graphically represents the ZOI obtained by plotting an average value of multiple experiments through the disc diffusion method. Herein, the results obtained using the different metal oxide combinations against the fungi and various bacterial strains are quite interesting. AZ which is the combination of elemental Ag_2O/Ag and ZnO had a good antifungal and antibacterial efficiency. Both the metal oxide had the capability to reduce the growth of fungi and bacteria together compared to the ZnO alone.

Further to qualify the materials synthesized in this work for biomedical applications, the MIC values have been evaluated. MIC is the minimum concentration of compound or drug which inhibits the growth of bacteria.[66] *A. baumannii* was chosen to study the MIC as it exhibited higher ZOI value compared to the other bacterial and fungal strains. From the above results, it can be seen that the MIC values obtained for the mixed oxide are very low compared to the results obtained for single oxide (Table 2). Furthermore, it can be noted that AZ (ZnO−Ag_2O/Ag) and SZ (ZnO−SnO_2) show excellent

Table 2. MIC Values Obtained for Different Samples

materials	Z (ZnO)	CZ (ZnO−CuO)	AZ (ZnO−Ag/Ag_2O)	SZ (ZnO−SnO_2)	A (Ag/Ag_2O)	C (CuO/Cu_2O)	S (SnO_2)
E_g (band energy), eV	3.25	2.15	1.98	3.12		2−2.4 (1.2 CuO)	3.6
MIC values (μg/mL)	0.312	0.312	0.010	0.019	0.039	1.25	1.25

https://doi.org/10.1021/acsomega.1c04139
ACS Omega 2021, 6, 31615−31631

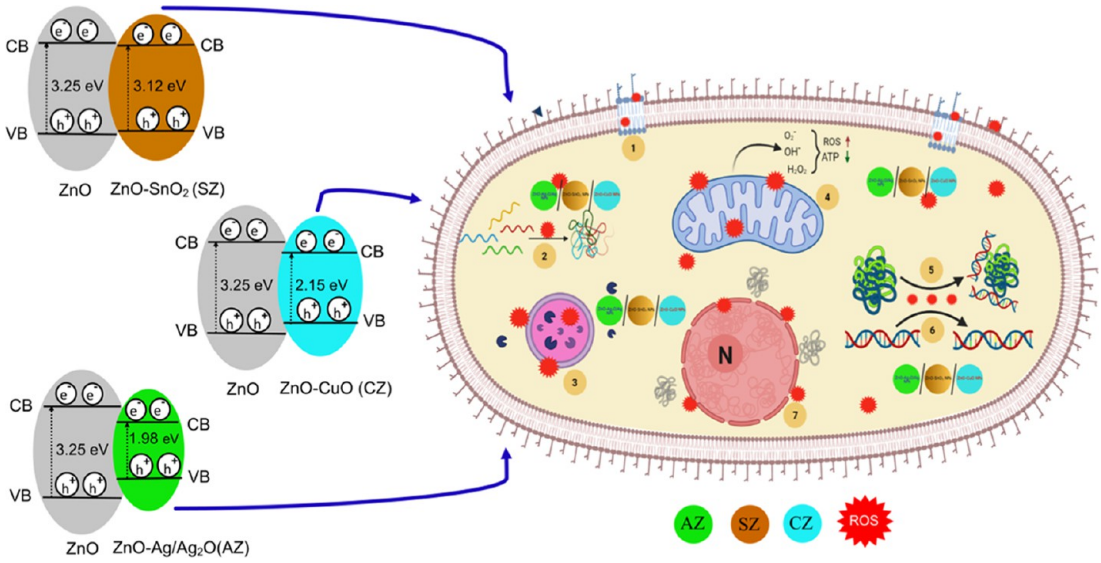

Figure 10. Schematic representation shows the change in the band energy gap for different composite NP systems and mechanisms involved in the bacterial cell wall damage through the ROS generation responsible for the MIC (Table 2).

MIC values of 0.010 and 0.019 μg/mL, respectively. Thus, it can be concluded that the AZ and SZ have maximum killing efficiency compared to the CZ (CuO−ZnO), A (Ag_2O/Ag), C (CuO), S (Sn/SnO_2), and Z (ZnO), as shown in Table 2. Thus, we can conclude that the present antibacterial materials also follow the ROS mechanism which subsequently has been shown in Figure 10. If we compared the band energy gap (E_g), then it is observed that ZnO−AgO_2/Ag had the lowest value of 1.98 eV and exhibited maximum antimicrobial activities compared to the ZnO−CuO (E_g: 2.15 eV) and ZnO−SnO_2 (E_g: 3.12 eV). Therefore, E_g may have a good relation for antimicrobial activities.

CONCLUSIONS

Bimetallic oxide composites NPs have been synthesized in the absence of any surfactant for broad spectrum applications. The "*in silico*" investigation for targeted proteins with these NPs and their nature of interactions have been studied for the determination of NP-mediated antibacterial and antifungal activities. Molecular docking studies predicted the binding affinity of composite NPs to their molecular target proteins of microbes, and the study revealed that the composite NPs enhanced the antimicrobial activities compared to the single metal/metal oxide NPs. For the conformation of enhanced antibacterial and antifungal activities of the synthesized composite NPs against the drug resistance, we have found out interaction using quorum-sensing PqsR,[34] RstA response regulator,[38] and FosA gene involved in multidrug resistance development.[37] An *in vitro* study revealed that the antimicrobial activity significantly improved with the use of composite NPs instead of single oxide NPs alone even in very low concentration of the sample used. Significantly, combination of the metallic Ag/Ag_2O and ZnO system gives the best results as antifungal and antibacterial materials. The combination of two metals/metal oxide composite NP systems undoubtedly enhanced the antimicrobial efficacy due to the cooperative electronic interactions between the NPs and targeted virulence/quorum-sensing proteins. Based on these results, it can be concluded that these materials can be used in broad prospective development of the healthcare technology, for preventing the biofilm formation and to prevent the growth of infections caused by the microorganisms. Furthermore, these NPs could act as potential antimicrobial agents against the resistance of drugs and could be effective in fabricating the personal protective kits for the healthcare management. However, authors are committed for the detailed studies on the action mechanism and *in vivo* studies which will be communicated later.

EXPERIMENTAL SECTION

Materials. Zinc chloride anhydrous ($ZnCl_2$) (M_w: 136.3 g mol^{-1}), stannous chloride ($SnCl_2{\cdot}2H_2O$) (M_w: 225.64 g mol^{-1}), cupric chloride A.R ($CuCl_2{\cdot}2H_2O$) (M_w: 170.48 g mol^{-1}), silver chloride extra pure AR (AgCl) (M_w: 143.32 g mol^{-1}), sodium borohydrate extrapure ($NaBH_4$) (M_w: 37.83 g mol^{-1}), and methanol (CH_3OH) were purchased from NICE Chemicals Ltd. and used without further purification. Sodium phosphate monobasic (119.98 gm/mol), sodium phosphate dibasic (141.96 g/mol), NaCl (58.44 g/mol), potassium chloride (74.55 g/mol), and 1 M sodium hydroxide solution (40 g/mol) purchased from Himedia Ltd. have been used for phosphate buffer and solution preparation. The mixed oxide NPs prepared for this work have been filed for the application of Indian Patents.[40,41] However, the brief of the synthesis methods has been provided as below.

Synthesis of Zinc Oxide (ZnO) NPs. In brief, 10 mmol of $ZnCl_2$ was added in 50 mL of alcohol under continuous stirring. Simultaneously, 20 mmol of $NaBH_4$ was added in 10 mL of alcohol under ice bath. Furthermore, $NaBH_4$ solution was added dropwise at the rate of 1 drop/2 s in the solution of zinc chloride under continuous stirring (300 rpm). The color change from transparent to milky white was observed. The solution was centrifuged (8000 rpm) and washed with deionized (DI) water three times and dried overnight at 80 °C. This sample is designated as Z (ZnO).

Synthesis of Zinc Copper Bimetallic Oxide NPs (ZnO−CuO). In brief, 10 mmol each of $ZnCl_2$ and $CuCl_2{\cdot}2H_2O$ was added in 50 mL of alcohol under continuous stirring (300 rpm) at room temperature (RT). 50 mmol of $NaBH_4$ was added in 20 mL of alcohol, and the exothermic reaction was

https://doi.org/10.1021/acsomega.1c04139
ACS Omega 2021, 6, 31615−31631

taken place at RT under ice bath. The solution was added dropwise at the rate of one drop per 2 s to the first solution. The color changed from greenish to dark green more like shade of black. The solution was centrifuged and washed with DI water thrice and dried overnight at 80 °C. Details of the synthesis method can be referred to the applications of Indian Patents.[40,41] This sample is designated as CZ (ZnO−CuO).

Synthesis of Zinc Silver Bimetallic Oxide NPs (ZnO−Ag_2O/Ag). In brief, chloride salts of silver and zinc were taken with same quantities as mentioned above, and the same procedure was adopted. After the dropwise addition of $NaBH_4$ solution, change in color from dark green to greenish black has been observed. The solution was centrifuged and washed with DI water three times and dried overnight at 80 °C.[40,41] This sample is designated as AZ (ZnO−Ag_2O/Ag).

Synthesis of Zinc Tin Bimetallic Oxide NPs (ZnO−SnO_2). In brief, 10 mmol of zinc and stannous chloride salts were taken, and the same procedure was followed as mentioned above. On addition of $NaBH_4$ solution, the color changed from milky transparent to brownish and then grayish. The solution was washed with DI water three times and dried overnight at 80 °C.[40,41] This sample is designated as SZ (ZnO−SnO_2).

Antibacterial Evaluation Study. *In Silico Molecular Interactions of Metallic Oxide NPs and the Target Protein of Microorganism.* Investigation of the molecular interaction of ZnO−Ag_2O/Ag, ZnO−CuO, and ZnO−SnO_2 and single oxide Ag, SnO_2, and Zn was carried out by applying Lamarckian genetic algorithms (GA) using AutoDock4.2 tool. Structures of the NPs were modeled and optimized using VESTA version 3, freely available software.[67] The crystal structure of quorum-sensing regulator PqsR (PDB ID: 4JVI), *P. aeruginosa*, response regulator RstA (PDB ID: 5E3J) *A. baumannii*, fosfomycin resistance protein (PDB ID: 5WEW) of *K. pneumoniae*, and heat shock protein 90 (HSP90) (PDB ID: 6CJP) of *C. albicans* were retrieved from protein data bank. Macromolecule preparation was carried by adding the polar hydrogen atoms, Kollman charges, and solvation parameter, and the defaulted grid box was generated. Computational flexible docking was performed using the optimized geometry of NPs and protein molecules. The docking parameter sets defaulted number of GA run set 30, and the maximum amount of generation was set at 27,000 for each study. Further analysis was conducted using AutoDock and Chimera software.

Disk Diffusion Method. For the disk diffusion method, we have selected one fungal strain, namely, *C. albicans* ATTC 90028 and some nosocomial bacterial strains [*K. pneumoniae* AT CC 700603, *P. aeruginosa* ATCC 27853, and *A. baumannii* (clinical strain)]. The modified procedure has been chosen for antibacterial activity. First, fresh microbial culture was made in normal saline (0.9%) to achieve two different concentrations of 10^6 and 10^8 cfu/mL. Sterile cotton swab was used to spread this prepared suspension, and it was left for drying for 5 min. Then, the sterile discs (Whatman filter paper no. 1) of size 4 mm diameter were placed on the medium surface. After that, 3 mg/mL of each of the nanomaterials was dispensed and then allowed to diffuse for 5 min. Then, the plates were incubated for 24 h at 37 °C. After the incubation, ZOI were measured around the discs. All the assays were conducted in triplicate, and statistically significant results were obtained.[66] Herein, 1, 2, 3, and 5 labels were used for the samples Z, CZ, SZ, and AZ, respectively, as shown in Figure 8.

Calculation of Minimum Inhibitory Concentration. The broth dilution method has been used to determine the MIC for *A. baumannii* as it showed better results among all the bacterial and fungal strain in our study.[68] Equal amounts of NPs were placed with different dilutions of cultured micro-organism. The nutrient broth was mixed in 96-well plates and incubated at 37 °C for 24 h. The preparation was carried out in a round-bottom microtiter plate containing 100 μL of diluted antibacterial nanomaterials. 10 different concentrations such as 10, 5, 2.5, 1.25, 0.625, 0.312, 0.156, 0.07, 0.03, and 0.019 μg/mL for each material were used for the experimentation. The MIC values were calculated based on the lowest concentration of the sample that prevent any noticeable growth of *A. baumannii*.

Luria Broth Dilution Method. The antibacterial activity of the samples Z, CZ, AZ, and SZ was investigated against *E. coli* strain DH5α by the Luria broth (LB) method. The stock solution was prepared by dispersing the NPs in DI water. In 10 mL of LB medium, bacterial culture was inoculated along with different concentrations with NPs and without NPs as control. Furthermore, the culture tubes were incubated at 37 °C in a shaker incubator at 3500 rpm for 12 h. OD values were measured at 600 nm at different time intervals and finally at 12 h.

Preparation of PB and PBS. In brief, a stock solution "A" was prepared by adding 13.8 g of sodium phosphate monobasic in 500 mL of dd-H_2O. Then, stock solution "B" was prepared by adding 26.81 g of sodium phosphate dibasic in 500 mL of dd-H_2O. Then, "A" and "B" were mixed well.

1× PB was prepared by adding 100 mL of stock solution of "A" with 400 mL of stock solution of "B," and 500 mL of dd-H_2O was added to make total 1 L.

1× PBS:10× PBS was prepared by adding 100 mL of stock solution of "A" with 400 mL of stock solution of "B," and then, 100 mL of 9% NaCl solution was added into another 400 mL of dd-H_2O. Furthermore, 1× PBS was prepared by mixing and adding 1 M potassium chloride and 1 M sodium hydroxide solution.

Characterization. UV−vis spectra were acquired between 190 and 800 nm using a UV−vis−NIR spectrometer (PerkinElmer: LAMBDA 750 instrument). The absorption of the prepared material was measured in a quartz cuvette of 1 cm optical path length. TEM images and SAED patterns were obtained using HRTEM (FEI Tecnai G2). Preparation of the HRTEM sample: a pinch of the samples was taken and dispersed in isopropanol and sonicated for 15 min. It was then drop cast on carbon-coated Cu grids (200 mesh). The elemental compositions were confirmed using the energy-dispersive X-ray spectrometer attached with the instrument. All the samples for FTIR (PerkinElmer) spectroscopy analysis were prepared by pelletizing with KBr (ratio 1:5) and with a scan range of 4000−400 cm^{-1}. The crystallinity of the nanomaterials was investigated using an X-ray diffractometer (Bruker AXS model D8) with a Cu Kα source (λ = 1.54 Å) with a step size of 0.02° and 2θ between 10 and 90°. Zeta potential was performed using a MS3000 model (Malvern Instruments Ltd, UK) to determine the distribution of the particle sizes. Zeta potential values were calculated using a Malvern Zetasizer (model: Zetasizer Nano ZSP) at RT. Furthermore, the BET method was used to calculate the surface area of the nanosized material. The N_2-adsorption−desorption experiments were performed at 76.5 K with an ASAP 2020 physisorption analyzer (Micromeritics Instrument

https://doi.org/10.1021/acsomega.1c04139
ACS Omega 2021, 6, 31615−31631

Corporation). The thermal stability, amount of heat flow, and phase transition were studied by TGA/DSC (Thermo ONIX Gaslab 300). The TG/DSC study was performed in an inert N_2 atmosphere from 30 to 1000 °C at a heating rate of 10 °C/min. To identify the elements present in the material, the XPS study was performed from 0 to 1200 eV using the Kratos Analytical AXIS Supra model.

Time-Scale Surface Zeta Potential and Stability Studies. The time-scale stabilities of the composite NPs were investigated for 7 days through zeta potential measurement considering defined time interval. Three sets of experiments were performed: (1) 5 μg/mL of each sample was prepared in 1× PBS for different pH values of 5, 6.9, 7.4, and 8 of ZnO and Ag/ZnO NPs. Similarly, (2) 5 μg/mL of each sample was prepared in PB solution for ZnO−Ag_2O/Ag−, ZnO−SnO_2, ZnO−CuO, and ZnO in pH 6.9 and 7.4, and (3) 5 μg/mL of each sample was dispersed in 0.9% w/v Saline solution. Finally, both DLS and zeta potential readings were taken for all of the above samples at different time intervals. The final results are tabulated in Tables S1−S4.

Time-Scale Dissolution Study through DLS. The time-scale dissolution and stabilities of the composite NPs were investigated for 7 days through DLS. The sample preparation has been conducted similar to the abovementioned zeta potential and stability study for ZnO−Ag_2O/Ag−, ZnO−SnO_2, ZnO−CuO, and ZnO in pH 5, 6.9, 7.4, and 8. Furthermore, DLS readings were taken for all the samples at different time intervals for up to 7 days. Before starting the measurement, all the samples were sonicated for 10 min to disperse. The final results are tabulated in Tables S5−S11.

Statistical Analysis. Data are expressed as mean values (±SD). Analysis of variance followed by Bonferroni post-test comparisons at different time intervals for multiple comparison tests in two-way ANOVA was carried out. In all cases, the p value was obtained from the ANOVA table, and the conventional 0.0001 level was considered to express the statistical significance.

■ ASSOCIATED CONTENT

Supporting Information

The Supporting Information is available free of charge at https://pubs.acs.org/doi/10.1021/acsomega.1c04139.

EDS spectrum, calculation of band gap (E_g) and diagrams, TGA results, DSC plots, FTIR spectra, XPS and antibacterial activity of NPs (bar diagram); zeta potential analysis; and DLS study and time-dependent dissolution analysis (PDF)

■ AUTHOR INFORMATION

Corresponding Author

Pradip Paik − *School of Biomedical Engineering, Indian Institute of Technology, Banaras Hindu University (BHU), Varanasi, Uttar Pradesh 221005, India;* orcid.org/0000-0001-7033-0636; Email: paik.bme@iitbhu.ac.in, pradip.paik@gmail.com

Authors

Monica Pandey − *School of Engineering Sciences and Technology, University of Hyderabad, Hyderabad, Telangana 500046, India*

Monika Singh − *School of Biomedical Engineering, Indian Institute of Technology, Banaras Hindu University (BHU), Varanasi, Uttar Pradesh 221005, India*

Kirti Wasnik − *School of Biomedical Engineering, Indian Institute of Technology, Banaras Hindu University (BHU), Varanasi, Uttar Pradesh 221005, India*

Shubhra Gupta − *School of Biomedical Engineering, Indian Institute of Technology, Banaras Hindu University (BHU), Varanasi, Uttar Pradesh 221005, India*

Sukanya Patra − *School of Biomedical Engineering, Indian Institute of Technology, Banaras Hindu University (BHU), Varanasi, Uttar Pradesh 221005, India*

Prem Shankar Gupta − *School of Biomedical Engineering, Indian Institute of Technology, Banaras Hindu University (BHU), Varanasi, Uttar Pradesh 221005, India*

Divya Pareek − *School of Biomedical Engineering, Indian Institute of Technology, Banaras Hindu University (BHU), Varanasi, Uttar Pradesh 221005, India*

Nyshadham Sai Naga Chaitanya − *Department of Animal Science, School of Life Sciences, University of Hyderabad, Hyderabad, Telangana 500046, India*

Somedutta Maity − *School of Engineering Sciences and Technology, University of Hyderabad, Hyderabad, Telangana 500046, India*

Aramati B. M. Reddy − *Department of Animal Science, School of Life Sciences, University of Hyderabad, Hyderabad, Telangana 500046, India*

Ragini Tilak − *Institute of Medical Sciences, Banaras Hindu University (BHU), Varanasi, Uttar Pradesh 221005, India*

Complete contact information is available at: https://pubs.acs.org/10.1021/acsomega.1c04139

Author Contributions

M.P. synthesized the materials and characterized them. K.W. and S.G. designed the *in silico* studies. M.P., M.S., and S.P. have performed the *in vitro* antimicrobial studies and decided the doses for treatments according to the *in silico* study and validated the results. P.S.G., D.P., and N.S.N.C. helped do the experiments at various levels. S.M. helped carry out the zeta analysis and dissolution studies through the zeta sizer. A.B.M.R. helped decide the pathogens. R.T. (medical practitioner) helped validate the results for medical usages. P.P. is the principle investigator and designed the whole project and monitored the same. All the authors contributed to write the manuscript and approved the submission.

Notes

The authors declare no competing financial interest.

■ ACKNOWLEDGMENTS

The authors acknowledge the research support grants awarded by DST-Nanomission, India (ref: SR/NM/NS-1005/2015) and Science and Engineering Research Board (SERB), India (ref: EEQ/2016/000040), awarded to P.P. Furthermore, M.P. acknowledges the CSIR-SRF fellowship awarded to her and support from Dr. R. K. Rana, IICT, Hyderabad, for extending scientific discussion for XPS and S. Pankaj Kumar for helping in doing TEM experiments.

■ REFERENCES

(1) Mahira, S.; Jain, A.; Khan, W.; Domb, A. J. *Chapter 1. Antimicrobial Materials-An Overview*; The Royal Society of Chemistry, 2019; pp 1−37.

(2) Raghunath, A.; Perumal, E. Metal Oxide Nanoparticles as Antimicrobial Agents: A Promise for the Future. *Int. J. Antimicrob. Agents* **2017**, *49*, 137−152.
(3) Dizaj, S. M.; Lotfipour, F.; Barzegar-Jalali, M.; Zarrintan, M. H.; Adibkia, K. Antimicrobial Activity of the Metals and Metal Oxide Nanoparticles. *Mater. Sci. Eng., C* **2014**, *44*, 278−284.
(4) Beyth, N.; Houri-Haddad, Y.; Domb, A.; Khan, W.; Hazan, R. Alternative Antimicrobial Approach: Nano-Antimicrobial Materials. *J. Evidence-Based Complementary Altern. Med.* **2015**, *2015*, 246012.
(5) Sirelkhatim, A.; Mahmud, S.; Seeni, A.; Kaus, N. H. M.; Ann, L. C.; Bakhori, S. K. M.; Hasan, H.; Mohamad, D. Review on Zinc Oxide Nanoparticles: Antibacterial Activity and Toxicity Mechanism. *Nano-Micro Lett.* **2015**, *7*, 219−242.
(6) Amininezhad, S.; Rezvani, A.; Amouheidari, M.; Amininejad, S.; Rakhshani, S. The Antibacterial Activity of SnO_2 Nanoparticles against Escherichia Coli and Staphylococcus Aureus. *Zahedan J. Res. Med. Sci.* **2015**, *17*, No. e1053.
(7) Prabhu, S.; Poulose, E. K. Silver Nanoparticles: Mechanism of Antimicrobial Action, Synthesis, Medical Applications, and Toxicity Effects. *Int. Nano Lett.* **2012**, *2*, 32.
(8) Hsueh, Y. H.; Tsai, P. H.; Lin, K. S. PH-Dependent Antimicrobial Properties of Copper Oxide Nanoparticles in Staphylococcus Aureus. *Int. J. Mol. Sci.* **2017**, *18*, 793.
(9) Wang, L.; Hu, C.; Shao, L. The Antimicrobial Activity of Nanoparticles: Present Situation and Prospects for the Future. *Int. J. Nanomed.* **2017**, *12*, 1227−1249.
(10) Azam, A.; Ahmed, A. S.; Oves, M.; Khan, M. S.; Memic, A. Size-Dependent Antimicrobial Properties of CuO Nanoparticles against Gram-Positive and -Negative Bacterial Strains. *Int. J. Nanomed.* **2012**, *7*, 3527−3535.
(11) Fakhri, A.; Behrouz, S.; Pourmand, M. Synthesis, Photocatalytic and Antimicrobial Properties of SnO_2, SnS_2 and SnO_2/SnS_2 Nanostructure. *J. Photochem. Photobiol., B* **2015**, *149*, 45−50.
(12) Radzig, M. A.; Nadtochenko, V. A.; Koksharova, O. A.; Kiwi, J.; Lipasova, V. A.; Khmel, I. A. Antibacterial Effects of Silver Nanoparticles on Gram-Negative Bacteria: Influence on the Growth and Biofilms Formation, Mechanisms of Action. *Colloids Surf., B* **2013**, *102*, 300−306.
(13) Zheng, K.; Setyawati, M. I.; Leong, D. T.; Xie, J. Antimicrobial Silver Nanomaterials. *Coord. Chem. Rev.* **2018**, *357*, 1−17.
(14) Perdikaki, A.; Galeou, A.; Pilatos, G.; Prombona, A.; Karanikolos, G. N. Ion-Based Metal/Graphene Antibacterial Agents Comprising Mono-Ionic and Bi-Ionic Silver and Copper Species. *Langmuir* **2018**, *34*, 11156−11166.
(15) Guo, B.-L.; Han, P.; Guo, L.-C.; Cao, Y.-Q.; Li, A.-D.; Kong, J.-Z.; Zhai, H.-F.; Wu, D. The Antibacterial Activity of Ta-Doped ZnO Nanoparticles. *Nanoscale Res. Lett.* **2015**, *10*, 336.
(16) Liu, Y.; He, L.; Mustapha, A.; Li, H.; Hu, Z. Q.; Lin, M. Antibacterial Activities of Zinc Oxide Nanoparticles against Escherichia Coli O157:H7. *J. Appl. Microbiol.* **2009**, *107*, 1193−1201.
(17) Reddy, L. S.; Nisha, M. M.; Joice, M.; Shilpa, P. N. Antimicrobial Activity of Zinc Oxide (ZnO) Nanoparticle against Klebsiella Pneumoniae. *Pharm. Biol.* **2014**, *52*, 1388−1397.
(18) Zarei, M.; Jamnejad, A.; Khajehali, E. Antibacterial Effect of Silver Nanoparticles against Four Foodborne Pathogens. *Jundishapur J. Microbiol.* **2014**, *7*, No. e8720.
(19) Sondi, I.; Salopek-Sondi, B. Silver Nanoparticles as Antimicrobial Agent: A Case Study on E. Coli as a Model for Gram-Negative Bacteria. *J. Colloid Interface Sci.* **2004**, *275*, 177−182.
(20) Mahapatra, O.; Bhagat, M.; Gopalakrishnan, C.; Arunachalam, K. D. Ultrafine Dispersed CuO Nanoparticles and Their Antibacterial Activity. *J. Exp. Nanosci.* **2008**, *3*, 185−193.
(21) Ahamed, M.; Alhadlaq, H. A.; Khan, M. A. M.; Karuppiah, P.; Al-Dhabi, N. A. Synthesis, Characterization, and Antimicrobial Activity of Copper Oxide Nanoparticles. *J. Nanomater.* **2014**, *2014*, 637858.
(22) Azam, A.; Ahmed, A. S.; Oves, M.; Khan, M. S.; Habib, S. S.; Memic, A. Antimicrobial Activity of Metal Oxide Nanoparticles against Gram-Positive and Gram-Negative Bacteria: A Comparative Study. *Int. J. Nanomed.* **2012**, *7*, 6003−6009.
(23) Ren, L.; Chen, D.; Hu, Z.; Gao, Z.; Luo, Z.; Chen, Z.; Jiang, Y.; Zhao, B.; Wu, C. M. L.; Shek, C.-H. Facile Fabrication and Application of SnO_2−ZnO Nanocomposites: Insight into Chain-like Frameworks, Heterojunctions and Quantum Dots. *RSC Adv.* **2016**, *6*, 82096−82102.
(24) Zhang, N.; Gao, Y.; Zhang, H.; Feng, X.; Cai, H.; Liu, Y. Preparation and Characterization of Core-Shell Structure of SiO_2@Cu Antibacterial Agent. *Colloids Surf., B* **2010**, *81*, 537−543.
(25) Sharma, M.; Hazra, S.; Basu, S. Synthesis of Heterogeneous Ag-Cu Bimetallic Monolith with Different Mass Ratios and Their Performances for Catalysis and Antibacterial Activity. *Adv. Powder Technol.* **2017**, *28*, 3085−3094.
(26) Perdikaki, A.; Galeou, A.; Pilatos, G.; Karatasios, I.; Kanellopoulos, N. K.; Prombona, A.; Karanikolos, G. N. Ag and Cu Monometallic and Ag/Cu Bimetallic Nanoparticle−Graphene Composites with Enhanced Antibacterial Performance. *ACS Appl. Mater. Interfaces* **2016**, *8*, 27498−27510.
(27) Alimunnisa, J.; Ravichandran, K.; Meena, K. S. Synthesis and Characterization of Ag@SiO_2 Core-Shell Nanoparticles for Antibacterial and Environmental Applications. *J. Mol. Liq.* **2017**, *231*, 281−287.
(28) Kumar, S.; Nigam, R.; Kundu, V.; Jaggi, N. Sol−Gel Synthesis of ZnO−SnO_2 Nanocomposites and Their Morphological, Structural and Optical Properties. *J. Mater. Sci. Mater. Electron.* **2015**, *26*, 3268−3274.
(29) Giusti, G.; Consonni, V.; Puyoo, E.; Bellet, D. High Performance ZnO-SnO_2:F Nanocomposite Transparent Electrodes for Energy Applications. *ACS Appl. Mater. Interfaces* **2014**, *6*, 14096−14107.
(30) Stankic, S.; Suman, S.; Haque, F.; Vidic, J. Pure and Multi Metal Oxide Nanoparticles: Synthesis, Antibacterial and Cytotoxic Properties. *J. Nanobiotechnol.* **2016**, *14*, 73.
(31) Yamamoto, O.; Ohira, T.; Alvarez, K.; Fukuda, M. Antibacterial Characteristics of $CaCO_3$−MgO Composites. *Mater. Sci. Eng., B* **2010**, *173*, 208−212.
(32) Vidic, J.; Stankic, S.; Haque, F.; Ciric, D.; Le Goffic, R.; Vidy, A.; Jupille, J.; Delmas, B. Selective Antibacterial Effects of Mixed ZnMgO Nanoparticles. *J. Nanopart. Res.* **2013**, *15*, 1595.
(33) Paszkiewicz, M.; Gołąbiewska, A.; Rajski, Ł.; Kowal, E.; Sajdak, A.; Zaleska-Medynska, A. Synthesis and Characterization of Monometallic (Ag, Cu) and Bimetallic Ag-Cu Particles for Antibacterial and Antifungal Applications. *J. Nanomater.* **2016**, *2016*, 2187940.
(34) Muimhneacháin, E. Ó.; Reen, F. J.; O'Gara, F.; McGlacken, G. P. Analogues of Pseudomonas Aeruginosa Signalling Molecules to Tackle Infections. *Org. Biomol. Chem.* **2018**, *16*, 169−179.
(35) Farrow, J. M., III; Wells, G.; Pesci, E. C. Desiccation Tolerance in Acinetobacter baumannii Is Mediated by the Two-Component Response Regulator BfmR. *PLoS One* **2018**, *13*, No. e0205638.
(36) Nabiel, Y.; Barakat, G. MurA, UhpT, GlpT and FosA Genes of Fosfomycin Resistance in Multi-Drug Resistant E. Coli Isolated from Hematological Malignancies' Patients with Blood Stream Infection. *Microbiol. Res. J. Int.* **2021**, *31*, 58−68.
(37) Tomich, A. D.; Klontz, E. H.; Deredge, D.; Barnard, J. P.; McElheny, C. L.; Eshbach, M. L.; Weisz, O. A.; Wintrode, P.; Doi, Y.; Sundberg, E. J.; Sluis-Cremer, N. Small-Molecule Inhibitor of FosA Expands Fosfomycin Activity to Multidrug-Resistant Gram-Negative Pathogens. *Antimicrob. Agents Chemother.* **2019**, *63*, No. e01524-18.
(38) Raorane, C. J.; Lee, J.-H.; Kim, Y.-G.; Rajasekharan, S. K.; García-Contreras, R.; Lee, J. Antibiofilm and Antivirulence Efficacies of Flavonoids and Curcumin Against Acinetobacter baumannii. *Front. Microbiol.* **2019**, *10*, 990.
(39) Gong, Y.; Li, T.; Yu, C.; Sun, S. Candida Albicans Heat Shock Proteins and Hsps-Associated Signaling Pathways as Potential Antifungal Targets. *Front. Cell. Infect. Microbiol.* **2017**, *7*, 520.
(40) Paik, P.; Pandey, M.; Patra, S.; Singh, M.; Wasnik, K.; Gupta, P. A Mesoporous Anti-Microbial Nanocomposite and a Method of

https://doi.org/10.1021/acsomega.1c04139
ACS Omega 2021, 6, 31615−31631

Preparation Thereof. Indian Patent Application No.: 202011031802, Dated: July 24, 2020, 2020.
(41) Paik, M.; Pandey, M.; Tilak, M. S. R. A Nanomaterial Based Antimicrobial Composition and a Method of Preparation Thereof. Indian Patent Application No.: 202011017968, Dated: April 27, 2020, 2020.
(42) Bankura, K.; Maity, D.; Mollick, M. M. R.; Mondal, D.; Bhowmick, B.; Roy, I.; Midya, T.; Sarkar, J.; Rana, D.; Acharya, K.; Chattopadhyay, D. Antibacterial Activity of Ag−Au Alloy NPs and Chemical Sensor Property of Au NPs Synthesized by Dextran. *Carbohydr. Polym.* **2014**, *107*, 151−157.
(43) Ethiraj, A. S.; Kang, D. J. Synthesis and Characterization of CuO Nanowires by a Simple Wet Chemical Method. *Nanoscale Res. Lett.* **2012**, *7*, 70.
(44) Das, I.; Sagadevan, S.; Chowdhury, Z. Z.; Hoque, M. E. Development, Optimization and Characterization of a Two Step Sol−Gel Synthesis Route for ZnO/SnO2 Nanocomposite. *J. Mater. Sci. Mater. Electron.* **2018**, *29*, 4128−4135.
(45) Bazant, P.; Sedlacek, T.; Kuritka, I.; Podlipny, D.; Holcapkova, P. Synthesis and Effect of Hierarchically Structured Ag-ZnO Hybrid on the Surface Antibacterial Activity of a Propylene-Based Elastomer Blends. *Materials* **2018**, *11*, 363.
(46) Cai, Z.; Kim, K.-K.; Park, S. Room Temperature Detection of NO2 Gas under UV Irradiation Based on Au Nanoparticle-Decorated Porous ZnO Nanowires. *J. Mater. Res. Technol.* **2020**, *9*, 16289−16302.
(47) Majeed Khan, M. A.; Kumar, S.; Ahamed, M.; Alrokayan, S. A.; AlSalhi, M. S. Structural and Thermal Studies of Silver Nanoparticles and Electrical Transport Study of Their Thin Films. *Nanoscale Res. Lett.* **2011**, *6*, 434.
(48) Honary, S.; Zahir, F. Effect of Zeta Potential on the Properties of Nano-Drug Delivery Systems - A Review (Part 1). *Trop. J. Pharm. Res.* **2013**, *12*, 265−273.
(49) Cherniakov, I.; Domb, A. J.; Hoffman, A. Self-Nano-Emulsifying Drug Delivery Systems: An Update of the Biopharmaceutical Aspects. *Expet Opin. Drug Deliv.* **2015**, *12*, 1121−1133.
(50) Xu, L.; Wei, B.; Liu, W.; Zhang, H.; Su, C.; Che, J. Flower-like ZnO-Ag_2O Composites: Precipitation Synthesis and Photocatalytic Activity. *Nanoscale Res. Lett.* **2013**, *8*, 536.
(51) Zhou, C.; Xu, L.; Song, J.; Xing, R.; Xu, S.; Liu, D.; Song, H. Ultrasensitive Non-Enzymatic Glucose Sensor Based on Three-Dimensional Network of ZnO-CuO Hierarchical Nanocomposites by Electrospinning. *Sci. Rep.* **2014**, *4*, 7382.
(52) Hoflund, G. B.; Hazos, Z. F.; Salaita, G. N. Surface Characterization Study of Ag, AgO, and Ag_2O Using x-Ray Photoelectron Spectroscopy and Electron Energy-Loss Spectroscopy. *Phys. Rev. B: Condens. Matter Mater. Phys.* **2000**, *62*, 11126−11133.
(53) Rashid, J.; Barakat, M. A.; Salah, N.; Habib, S. S. Ag/ZnO Nanoparticles Thin Films as Visible Light Photocatalysts. *RSC Adv.* **2014**, *4*, 56892−56899.
(54) Li, Z.; Zhou, Y.; Zhang, J.; Tu, W.; Liu, Q.; Yu, T.; Zou, Z. Hexagonal Nanoplate-Textured Micro-Octahedron Zn2SnO4: Combined Effects toward Enhanced Efficiencies of Dye-Sensitized Solar Cell and Photoreduction of CO_2 into Hydrocarbon Fuels. *Cryst. Growth Des.* **2012**, *12*, 1476−1481.
(55) Li, M.; Hu, Y.; Xie, S.; Huang, Y.; Tong, Y.; Lu, X. Heterostructured ZnO/SnO2−x Nanoparticles for Efficient Photocatalytic Hydrogen Production. *Chem. Commun.* **2014**, *50*, 4341−4343.
(56) Ren, J.; Wang, W.; Sun, S.; Zhang, L.; Wang, L.; Chang, J. Crystallography Facet-Dependent Antibacterial Activity: The Case of Cu_2O. *Ind. Eng. Chem. Res.* **2011**, *50*, 10366−10369.
(57) Aleksic, I.; Jeremic, J.; Milivojevic, D.; Ilic-Tomic, T.; Šegan, S.; Zlatović, M.; Opsenica, D. M.; Senerovic, L. N-Benzyl Derivatives of Long-Chained 4-Amino-7-Chloro-Quionolines as Inhibitors of Pyocyanin Production in Pseudomonas Aeruginosa. *ACS Chem. Biol.* **2019**, *14*, 2800−2809.
(58) Boopathi, S.; Vashisth, R.; Manoharan, P.; Kandasamy, R.; Sivakumar, N. Stigmatellin Y - An Anti-Biofilm Compound from Bacillus Subtilis BR4 Possibly Interferes in PQS-PqsR Mediated Quorum Sensing System in Pseudomonas Aeruginosa. *Bioorg. Med. Chem. Lett.* **2017**, *27*, 2113−2118.
(59) Kumar, L.; Chhibber, S.; Kumar, R.; Kumar, M.; Harjai, K. Zingerone Silences Quorum Sensing and Attenuates Virulence of Pseudomonas Aeruginosa. *Fitoterapia* **2015**, *102*, 84−95.
(60) Draughn, G. L.; Milton, M. E.; Feldmann, E. A.; Bobay, B. G.; Roth, B. M.; Olson, A. L.; Thompson, R. J.; Actis, L. A.; Davies, C.; Cavanagh, J. The Structure of the Biofilm-Controlling Response Regulator BfmR from Acinetobacter baumannii Reveals Details of Its DNA-Binding Mechanism. *J. Mol. Biol.* **2018**, *430*, 806−821.
(61) Russo, T. A.; Manohar, A.; Beanan, J. M.; Olson, R.; MacDonald, U.; GrahamUmland, J. T. C. The Response Regulator BfmR Is a Potential Drug Target for Acinetobacter baumannii. *mSphere* **2016**, *1*, No. e00082-16.
(62) Whitesell, L.; Robbins, N.; Huang, D. S.; McLellan, C. A.; Shekhar-Guturja, T.; LeBlanc, E. V.; Nation, C. S.; Hui, R.; Hutchinson, A.; Collins, C.; Chatterjee, S.; Trilles, R.; Xie, J. L.; Krysan, D. J.; Lindquist, S.; Porco, J. A.; Tatu, U.; Brown, L. E.; Pizarro, J.; Cowen, L. E. Structural Basis for Species-Selective Targeting of Hsp90 in a Pathogenic Fungus. *Nat. Commun.* **2019**, *10*, 402.
(63) Yuan, R.; Tu, J.; Sheng, C.; Chen, X.; Liu, N. Effects of Hsp90 Inhibitor Ganetespib on Inhibition of Azole-Resistant Candida Albicans. *Front. Microbiol.* **2021**, *12*, 1280.
(64) Xia, T.; Kovochich, M.; Liong, M.; Mädler, L.; Gilbert, B.; Shi, H.; Yeh, J. I.; Zink, J. I.; Nel, A. E. Comparison of the Mechanism of Toxicity of Zinc Oxide and Cerium Oxide Nanoparticles Based on Dissolution and Oxidative Stress Properties. *ACS Nano* **2008**, *2*, 2121−2134.
(65) Raghupathi, K. R.; Koodali, R. T.; Manna, A. C. Size-Dependent Bacterial Growth Inhibition and Mechanism of Antibacterial Activity of Zinc Oxide Nanoparticles. *Langmuir* **2011**, *27*, 4020−4028.
(66) Joshi, R.; Yadav, S. K.; Mishra, H.; Pandey, N.; Tilak, R.; Pokharia, S. Interaction of Triorganotin(IV) Moiety with Quinolone Antibacterial Drug Ciprofloxacin: Synthesis, Spectroscopic Investigation, Electronic Structure Calculation, and Biological Evaluation. *Heteroat. Chem.* **2018**, *29*, No. e21433.
(67) Momma, K.; Izumi, F. VESA3 for Three-Dimensional Visualization of Crystal, Volumetric and Morphology Data. *J. Appl. Crystallogr.* **2011**, *44*, 1272−1276.
(68) Zulfikar, A. H. M.; Siddiqua, M.; Nahar, L.; Habib, M. D. R. N.; Uddin, N.; Hassan, N.; Rana, M. D. S. In Vitro Antibacterial, Antifungal & Cytotoxic Activity Of Scoparia Dulcis L. *Int. J. Pharm. Pharmaceut. Sci.* **2011**, *3*, 198−203.

https://doi.org/10.1021/acsomega.1c04139
ACS Omega 2021, 6, 31615−31631